NASA Technical Memorandum 102842

Experimental Study of an Independently Deflected Wingtip Mounted on a Semispan Wing

D. M. Martin and L. A. Young

September 1991

NASA

National Aeronautics and
Space Administration

Experimental Study of an Independently Deflected Wingtip Mounted on a Semispan Wing

D. M. Martin, University of Kansas Center for Research, Inc., Lawrence, Kansas
L. A. Young, Ames Research Center, Moffett Field, California

September 1991

NASA

National Aeronautics and
Space Administration

Ames Research Center
Moffett Field, California 94035-1000

TABLE OF CONTENTS

NOMENCLATURE

B — wind tunnel breadth

$C_{D_{form}}$ — form drag component of C_{D_T}

C_{D_i} — induced drag component (resulting from lift) of C_{D_T}

$C_{D_{itf}}$ — interference component of C_{D_T}

$C_{D_{sf}}$ — skin-friction component of C_{D_T}

C_{D_T} — tip drag coefficient, $D_T/qS_T c_T$

C_{D_0} — C_{D_T} for $\alpha_T = 0.0°$

C_{L_T} — tip lift coefficient, $L_T/qS_T c_T$

C_{L_α} — variation of tip lift coefficient with angle of attack, $\partial C_{L_T}/\partial \alpha_T$, rad^{-1} or deg^{-1}

C_{L_0} — C_{L_T} for $\alpha_T = 0.0°$

$C_{m_{ac}}$ — tip pitching moment coefficient about the tip aerodynamic center

C_{m_q} — change in tip pitching moment coefficient with tip pitch rate

$C_{m_q}[...]$ — response of pitching moment coefficient to unit step change in q

C_{m_T} — tip pitching moment coefficient about quarter-chord point of inboard wing, $M_T/qS_T c_T$

C_{m_α} — variation of tip pitching moment coefficient with angle of attack, $\partial C_{m_T}/\partial \alpha_T$, rad^{-1} or deg^{-1}

$C_{m_\alpha}[...]$ — response of pitching moment coefficient to unit step change in α

$C_{m_{\dot\alpha}}$ — tip pitch damping coefficient, $\partial C_{m_T}/\partial(\dot\alpha_T c_T/V_\infty)$

C_{m_0} — C_{m_T} for $\alpha_T = 0°$

C_{m_0} — C_{m_T} for $C_{L_T} = 0$

$C_{m_{0.0}}$	C_{m_x} at $x = 0.0$
c_T	tip inboard chord length, ft
D_T	tip drag force in wind axis system, lb
H	wind tunnel height
$\dot{h}_T$	tip vertical velocity component caused by plunging motion, ft/sec
I_α	tip mass moment of inertia about pitch axis, ft-lb sec^2
K_s	tip torsional spring constant, ft-lb
L_T	tip lift force in wind axis system
M_T	tip pitching moment, measured about inboard wing quarter-chord point, ft-lb
N	measured normal force, lb
q	dynamic pressure, psf
q_T	pitch rate, rad/sec
Re	Reynolds number based on tip root chord, $\rho V_\infty c_T / \mu$
RM	measured rolling moment, ft-lb
S	measured side force, lb
S_T	tip reference area, ft^2
t_2	streamline curvature effect on angle of attack
V_∞	tunnel free-stream velocity, ft/sec
x	chordwise direction in wing-fixed coordinate system
x_{ac}	chordwise position of the tip aerodynamic center
y	spanwise wing station, ft
α_T	tip angle of attack
α_W	wing angle of attack

$(\Delta C_L)_{SC}$ lift correction for streamline curvature

$(\Delta\alpha)_{dw}$ angle-of-attack correction for downwash

$(\Delta\alpha)_{sc}$ angle-of-attack correction for streamline curvature

$\Delta\theta$ tip incidence angle relative to inboard wing, $\alpha_T - \alpha_W$, rad or deg

ε velocity increment

ε_{sb} velocity correction for solid-body blockage

ε_{wb} velocity correction for wake blockage

θ_p mechanical spring pretwist angle, rad or deg

θ_T tip incidence angle relative to horizontal reference plane

μ coefficient of viscosity, slug/ft-sec

ρ sea-level air density, slug/ft^3

SUMMARY

The results of a subsonic wind tunnel test of a semispan wing with an independently deflected tip surface are presented and analyzed. The tip surface was deflected about the quarter-chord of the rectangular wing and accounted for 17% of the wing semispan. The test was conducted to measure the loads on the tip surface and to investigate the nature of aerodynamic interference effects between the wing and the deflected tip. Results are presented for two swept tip surfaces of similar planform but different airfoil distributions. The report contains plots of tip lift, drag, and pitching moment for various Reynolds numbers and tip deflection angles with respect to the inboard wing. Oil flow visualization photographs for a typical Reynolds number are also included. Important aerodynamic parameters such as lift and pitching moment slopes and tip aerodynamic center location are tabulated. A discussion is presented of the relationship between tip experimental data acquired in a steady flow and the prediction of unsteady tip motion at fixed-wing angles of attack.

INTRODUCTION

The Free-Tip Rotor concept was developed to reduce both the tip oscillatory loading of helicopter blades and the rotor power requirement (ref. 1). This configuration consists of a helicopter blade with the last 10% of the length allowed to pitch freely as a rigid body about the quarter-chord point of the inboard blade. The free-pitching tip is designed to respond to local changes in inflow and thus reduce the amplitude of azimuthally varying tip loads. Because of its simplicity, a nonrotating semispan wing with an independently deflected tip is ideal for studying the aerodynamic interactions between the wing and the tip. The deflected tip can be described as a completely separate tip surface attached to the inboard wing with minimal spanwise gap, at an angle of incidence that can be varied independently. In this simplified model, the tip is constrained and the angle of incidence is fixed while the loads are measured in a steady flow.

Since a detailed knowledge of tip aerodynamics in subsonic flow is required for design purposes, a series of tests has been carried out to measure aerodynamic loads on both wing and tip surfaces (refs. 2–4). During these tests, the tip planforms were first-generation concepts that used V23010 airfoil sections. A new family of tip planforms has been developed in the last few years (ref. 5); these incorporate advanced-technology airfoils and geometries that are more compatible with desired rotor aerodynamic performance. This report contains the results of a wind tunnel test of a semispan wing fitted with these advanced tip planforms.

The present study is part of the continuing research program associated with the Free-Tip Rotor concept. The data presented in this report will be used to define the rotor blade design of an Advanced Free-Tip Rotor (AFTR) small-scale wind tunnel model. The report contains plots of tip lift, drag, and pitching moment coefficients for different values of tip incidence angle with respect to the inboard wing. Oil flow visualization results and some important design parameters, such as aerodynamic center location, are briefly discussed, and calculations of zero-angle-of-attack lift and pitching moment coefficients are reported. Possible uses of the measured data as applied to oscillating tips in unsteady flow are also proposed.

TEST OBJECTIVES

The objectives of this test were as follows:

1. To measure the lift, pitching moment, and drag of the new tip planforms in subsonic flow, and to investigate the effect of the tip incidence angle, measured with respect to the wing ($\Delta\theta$)

2. To compute the lift and pitching moment slopes, and the aerodynamic center location, for each planform

3. To study flow patterns on upper and lower tip surfaces and thus qualitatively identify the induced aerodynamic effects of the inboard wing on the tip

EXPERIMENTAL APPARATUS AND PROCEDURES

This test was conducted in the Ames 7- by 10-Foot Subsonic Wind Tunnel. Tip aerodynamic forces were measured with a 3/4-in.-diameter, six-component, internal strain-gauge balance. The balance was mounted at the quarter-chord point of the inboard wing. Wing aerodynamic loads were not measured.

Model Description and Assembly

Two new tip configurations were tested; these are subsequently referred to as the RC10/08 tip and the RC10/05 tip. The two tips had the same planform shape and dimensions (fig. 1), but different airfoil section distributions. Three section profiles were used; they were based on new airfoil designs optimized for high lift and low drag in transonic flow. The airfoil surface coordinates are listed in tables A1, A2, and A3 in appendix A. Both tips consisted of three separate regions: an inboard area swept 10° with 10%-thick airfoils, a transition region, and an outboard portion with thinner airfoil sections. The transition and outboard regions were highly swept. The airfoil sections of the RC10/08 tip decreased in thickness from the 10%-thick RC10 to the 8%-thick RC08 over 18.8% of the tip span (fig. 1). On the RC10/05 tip, the thickness decreased from 10% to 5% over 9.4% of the span length. The span of both tips was 0.776 ft, and their planform areas were 0.40 ft^2.

The semispan wing consisted of two parts. The first was a solid steel, rectangular inboard portion with V23010 airfoil section profiles and a nonlinear twist distribution. The V23010 airfoil-surface coordinates are listed in table A4, and the wing twist distribution is plotted in figure A1 of appendix A. The second part was a nonmetric balsa-wood balance housing that matched the inboard section profiles, thus extending the wing inboard span. The wing semispan and area, without tip surfaces, were 3.79 ft and 2.60 ft^2, respectively. The wing had a semispan aspect ratio of 5.52 and a chord length of 0.686 ft, and was mounted vertically in the test section. A sketch of the wing and tip showing the internal balance location and wing-fixed coordinate system is shown in figure 2.

2

The tips were attached to the wing as follows: Before the tip was mounted onto the steel wing, the balance was inserted into a cylindrical sleeve with a shank attached to one end. The balance/sleeve assembly was then partially inserted into the wing at its quarter-chord point. The tip was then mounted over the sleeve, and set screws were placed into the shank to set the tip incidence angle with respect to the wing. Several set-screw holes were used to allow various tip deflection angles.

The moment reference center and the pitch axis, about which tip incidence angles with respect to the wing were set, lie at the quarter-chord of the wing section at the interface between the balsa-wood insert and the tip surface (fig. 2). The wing angle of attack was measured with respect to the x axis at this location. Figure 3 shows the complete assembly in the tunnel test section. The span of the entire configuration was 4.57 ft; its semispan aspect ratio was 6.96. The tip planform span accounted for 17.2% of the total configuration semispan.

Test Conditions and Procedures

The test conditions and ranges of wing and tip angles of attack are listed in table 1. The dynamic pressure was varied in increments of 5 psf. The maximum Mach number achieved was 0.13. As shown in table 1, three values of tip incidence angle with respect to the wing were used for the RC10/05 tip and four values for the RC10/08 tip. These were determined from the most feasible set-screw positions, given mechanical constraints and design considerations. The data were acquired by first setting the tip incidence angle relative to the inboard wing and then varying the wing angle of attack. Therefore, since $\Delta\theta$ was fixed for a given run, the tip geometric angle of attack (α_T) varied by the same amount as the wing geometric angle of attack (α_W).

Table 1. Test conditions and ranges of parameters

Parameter	Value
Dynamic pressure	$5\ psf \le q \le 25\ psf$
Reynolds number	$2.76 \times 10^5 \le Re \le 6.18 \times 10^5$
Wing angle of attack	$0.0° \le \alpha_W \le 16.7°$
Tip angle of attack	$-5.26° \le \alpha_T \le 18.2°$
Tip incidence angle	
RC10/08	$\Delta\theta = 1.5°, -3.5°, -9.0°, -13.0°$
RC10/05	$\Delta\theta = -2.5°, -8.0°, -10.0°$

The V23010 airfoil coordinates listed in table A4 of appendix A were defined in terms of a reference line bisecting the upper and lower surfaces of the trailing edge (fig. 4). The wing angles of attack specified throughout this report were measured from this reference line, since it coincides with the wing-fixed x axis. Figure 4 shows a view looking inboard at the wing with the tip removed. The orientation of the balance axes is also shown. Since the balance axes are rotated with the wing angle of attack, the tip lift, drag, and pitching moment were computed in the wind axis system as follows:

$$L_T = N\cos\alpha_W + S\sin\alpha_W$$
$$D_T = N\sin\alpha_W + S\cos\alpha_W \tag{1}$$
$$M_T = -RM$$

Corrections

The data presented here have been corrected for tunnel wall and blockage effects. These corrections are outlined in detail in appendix B. Since the data were acquired at relatively low dynamic pressure and load levels, no corrections were applied to account for balance deformations.

RESULTS

The data are presented as plots of C_{L_T} vs α_T (lift curves), C_{D_T} vs C_{L_T} (drag polars), and C_{m_T} vs α_T and C_{m_T} vs C_{L_T} (pitching moment curves). These plots are drawn for several Reynolds numbers at constant tip incidence angles ($\Delta\theta$) and for various tip incidence angles at constant Reynolds numbers. Some poor-quality data were omitted from the plots, so the number of curves or data points may not correspond from one plot to another for equivalent test conditions or runs.

For lift curves and drag polars, the data were fitted by first- and second-order least squares, respectively. For tip lift data the curves were fitted only to points corresponding to the linear range of the lift coefficient: beyond the stall point, only the data points are shown. The accuracy of force and moment coefficients was estimated from known balance gauge accuracies and from tolerances associated with other measured parameters, such as dynamic pressure, reference lengths and areas, etc. The estimated combined accuracies were calculated as percentages of the reduced data values as follows: for C_{L_T}, $\pm1.84\%$; for C_{D_T}, $\pm1.84\%$; and for C_{m_T}, $\pm1.77\%$.

Finally, although two tip planforms were tested, no attempt is made here to compare and rate the aerodynamic performance of the tips. The test was not carried out with this objective in mind. One of the main purposes of this experiment was to determine the effect of the $\Delta\theta$ parameter for a given tip. This approach yields important information on the mutually induced aerodynamic effects between the wing and the tip.

Reynolds Number Effects

An analysis of the data plotted at constant $\Delta\theta$ for different Reynolds numbers illustrates some important aerodynamic characteristics of the unique type of configuration discussed in this report. Figure 5 shows, for the RC10/08 tip, the variation of tip lift coefficient with angle of attack (fig. 5(a)) and the related drag polars (fig. 5(b)), for $\Delta\theta = -3.5°$. As expected, the lift curve slopes ($\partial C_{L_T} / \partial\alpha_T$) do not vary a great deal, and a slight effect of Reynolds number on C_{L_0} (C_{L_T} for $\alpha_T = 0.0°$) is observed in figure 5(a). The curve for $Re = 2.76 \times 10^5$ shows the classic stall break in the vicinity of $\alpha_T = 12.0°$.

The drag polars of figure 5(b) show the differences in drag loads between the higher and lower values of Reynolds number. Many factors play a role in these results and in the drag plots that follow in this section. A better understanding can be gained by reviewing the drag buildup process in greater detail.

The total tip drag for this type of configuration may be expressed in terms of its four main components:

$$C_{D_T} = C_{D_0} + C_{D_i} = C_{D_{form}} + C_{D_{sf}} + C_{D_{itf}} + C_{D_i} \tag{2}$$

The levels of induced drag (C_{D_i}) are expected to be similar for points on different C_{D_T} vs C_{L_T} curves with the same lift coefficient. The large difference between the curve for $Re = 2.76 \times 10^5$ and the other curves in figure 5(b) is probably related to the transition from laminar to turbulent flow. Reference 6 lists the flat-plate transition Reynolds number as somewhere between 3.5×10^5 and 10×10^5. For $Re = 3.91 \times 10^5$ and above, the turbulent region in the boundary layers probably grows and thus increases the $C_{D_{sf}}$ component in equation (2). Also, turbulent boundary layers are generally thicker than laminar ones (ref. 6); this allows greater interaction between the lifting surfaces and may increase the $C_{D_{itf}}$ term in equation (2). In particular, the increase in $C_{D_{itf}}$ could occur when the tip caps of the two surfaces (facing each other across the small gap) are very close, such as for $\Delta\theta = -3.5°$.

Figure 6 shows the lift (fig. 6(a)) and drag (fig. 6(b)) trends of the RC10/08 tip for $\Delta\theta = -13.0°$. Figure 6(a) shows a loss of lift for $Re = 2.76 \times 10^5$, probably caused by partial flow separation, and subsequent reattachment, at a very low tip angle of attack. At this value of $\Delta\theta$, when $\alpha_T = 0.0°$, then $\alpha_W = 13.0°$, and the separation effect is related to the upwash of the inboard wing, which increases the loading on the tip surface. The separation and reattachment shown in figure 6(a) shows the high sensitivity of the flow to disturbances at low Reynolds numbers.

Also, it is apparent from figure 6(a) that for a slightly higher Reynolds number ($Re = 3.91 \times 10^5$), the flow is able to overcome adverse pressure gradients near the trailing edge, thus resulting in a more gradual loss of lift. The associated drag polar in figure 6(b) shows that in the range $0.1 \leq C_{L_T} \leq 0.5$ there is little Reynolds number effect. The drag data acquired for $Re = 2.76 \times 10^5$ at this tip incidence angle were too unreliable to be shown here.

Figures 7 and 8 show the lift curves and drag polars for the RC10/05 tip at $\Delta\theta = -2.5°$ and $\Delta\theta = -10.0°$, respectively. Again, the lift-curve slopes of figure 7(a) remain approximately constant over the range of Reynolds numbers shown, although the sensitivity of C_{L_0} to Reynolds number is more obvious than for the RC10/08 tip. Separation is observed for the lowest Reynolds number at $\Delta\theta = -2.5°$, with one data point indicating possible reattachment. The drag polars in figure 7(b) are grouped together and show little evidence of a trend caused by a change in Reynolds number. Figure 8(a) shows the premature stall associated with the stronger upwash at $\Delta\theta = -10.0°$ and $Re = 2.76 \times 10^5$ ($\alpha_T = 6.0°$, $\alpha_W = 16.0°$). Also, as before, a Reynolds number of 3.91×10^5 is high enough to delay separation.

5

The drag polars of figure 8(b) ($\Delta\theta = -10.0°$) show much higher sensitivity to Reynolds number than those of previous cases; for a constant value of C_{L_T}, as Re increases, C_{D_T} also increases. This seems to occur for values of C_{L_T} from 0.1 to 0.6. As explained above, the subtle contributions of skin friction versus interference drag cannot be extracted from these data. The spread in the curves of figure 8(b) are more consistent than the spread in the curves for the RC10/08 tip (figs. 5(b) and 6(b)); this may be related to local pressure gradients, which also have a strong influence on the location of the transition point. As will be discussed later, the wing upwash has a substantial impact on the tip-surface pressure distribution. Thus, these trends must be due to increases in $C_{D_{sf}}$ and $C_{D_{itf}}$.

Tip Incidence Angle ($\Delta\theta$) Effects

RC10/08 Tip

Some of the aerodynamic benefits derived from this configuration can be readily understood by comparing values of C_{L_T} and C_{D_T} for different values of $\Delta\theta$. Figures 9 and 10 show lift curves and drag polars for the RC10/08 tip at Reynolds numbers of 4.79×10^5 and 5.53×10^5, respectively. For a given angle of attack, the lift produced by the tip increases as the negative value of $\Delta\theta$ increases. This is caused by the upwash effect of the wing vortex, which increases the local aerodynamic angle of attack across the span of the tip.

For a given value of α_T, the value of α_W actually increases with larger negative values of $\Delta\theta$ ($\alpha_W = -\Delta\theta + \alpha_T$). For large α_W, the wing loading is high, resulting in a strong wingtip vortex (actually shed at the junction between wing and tip surfaces) and thus a high loading on the tip. For example, at $\alpha_T = 0.0°$ and $\Delta\theta = -13.0°$, then $\alpha_W = 13.0°$ and figure 9(a) shows that the wing loading is very high. For the same α_T, as $\Delta\theta$ is reduced to $-9.0°$ ($\alpha_W = 9.0°$) and then to $-3.5°$ ($\alpha_W = 3.5°$), C_{L_T} is reduced accordingly. The plots only show points in the lower range of lift coefficient. This is because of concerns regarding allowable loads on the internal balance and its attachment point at high dynamic pressures.

The drag plot (fig. 9(b)) shows that if a constant value of C_{L_T} is considered, C_{D_T} decreases as $\Delta\theta$ increases negatively from $1.5°$ to $-9.0°$. This again is related to the reduction of induced drag that results from the stronger upwash associated with higher negative $\Delta\theta$. It was shown through the use of a panel method code in reference 5 that this effect occurred consistently for negative $\Delta\theta$. However, because of the limitations of the numerical model, only induced drag was computed. The exception of figure 9(b) is that the drag curve for $\Delta\theta = -13.0°$ lies above that for $\Delta\theta = -9.0°$, indicating a higher level of drag for the same tip lift. Although the differences are small, the drag polars of figure 10(b) (at the higher Reynolds number) also show that less drag was measured at $\Delta\theta = -3.5°$ than at $\Delta\theta = -13.0°$ for values of C_{L_T} below 0.3. Although fewer data points are available at Re $= 5.53 \times 10^5$ and q $= 20$ psf, the curves of figure 10 show essentially the same trends as those of figure 9.

Figure 11 shows the variation of tip pitching moment with lift for the RC10/08 tip at both test conditions (Re $= 4.79 \times 10^5$ and 5.53×10^5) considered above. In both cases, for a constant value of C_{L_T}, the pitching moment is less negative for larger negative $\Delta\theta$. The reason for this is related to the strength of the wing vortex and its position relative to the tip surface. At negative $\Delta\theta$, the tip trailing

edge lies above the wing trailing edge, so the vortex shed from the wing/tip junction acts primarily on the lower surface of the tip. Since for constant C_{L_T}, α_W is larger for larger negative values of $\Delta\theta$, the wing vortex strength and associated suction are also greater. Because the lower pressure region acts on the lower tip surface aft of the moment reference center, the resulting change in pitching moment is in the nose-up direction, becoming less negative, as illustrated in figures 11(a) and (b).

Figure 12 shows the variation of tip pitching moment with tip geometric angle of attack. For constant α_T, the pitching moment is more negative for larger negative values of $\Delta\theta$. This is primarily related to the increased lift at negative $\Delta\theta$ illustrated in figures 9(a) and 10(a).

RC10/05 Tip

Figures 13 through 16 show the test results for the RC10/05 tip. As stated earlier, the only difference between the two tip surfaces is the type of airfoil sections used and their spanwise distribution. The results are presented here for Reynolds numbers of 2.76×10^5 and 3.91×10^5 (different from those discussed in the previous section) to verify the observations made at the higher Reynolds numbers. In figure 13(a) (Re = 2.76×10^5), all three curves show some loss of lift because of flow separation. Note that for $\Delta\theta = -8.0°$ and $-2.5°$, the flow reattaches, as indicated by the recoveries in lift beyond the initial separation point. Initial separation occurs in the same range of α_T for $\Delta\theta = -10.0°$ and $-8.0°$, because the upwash on the tip does not differ much between these two cases. For a given value of α_T, the upwash (and therefore the loading) on the tip is reduced for lower values of negative $\Delta\theta$, so the angle of incidence of the entire configuration (and therefore α_T) can be increased to a higher value before tip stall occurs, as seen in figure 13(a).

The drag plot for Re = 2.76×10^5 (fig. 13(b)) shows little difference between the $\Delta\theta = -10.0°$ and $\Delta\theta = -8.0°$ cases. Nonetheless, there is a large difference between the $\Delta\theta = -2.5°$ case and the $\Delta\theta = -10.0°$ and $-8.0°$ cases, further supporting the conclusion of a reduction in induced drag at higher negative $\Delta\theta$. The form drag for this tip is quite low (some of the airfoil sections are only 5% thick), and the total drag is reduced further by the drop in induced drag that results from the wing upwash. At optimum tip lift coefficients for $\Delta\theta = -8.0°$ and $-10.0°$, the tip drag loads were so small that they were below the sensitivity limit of the internal balance, hence the data points in the $C_{D_T} \approx 0.0$ range of figure 13(b).

Figure 14 shows lift and drag plots for Re = 3.91×10^5. In figure 14(b), the data indicate a reduction in drag with increasing negative $\Delta\theta$ for the range $-8.0° \leq \Delta\theta \leq -2.5°$. The curve for $\Delta\theta = -10.0°$ lies above that for $\Delta\theta = -8.0°$. Note the similarity in the trends of figures 14(b) and 9(b). This may indicate that there is indeed a limit to which $\Delta\theta$ can be increased negatively and still achieve a reduction in total drag. This effect is related to the relative magnitudes of the four terms in equation (2). As stated earlier, a detailed drag breakdown cannot be established because of the limited scope of this test.

The pitching moment curves of figures 15 and 16 show essentially the same behavior as observed in figures 11 and 12 for the RC10/08 tip. Slight differences in the slopes $\partial C_{m_T}/\partial\alpha_T$ of figure 16 as $\Delta\theta$ changes can probably be attributed to experimental error.

Flow Visualization

The intent of the flow visualization runs was to study the surface-flow characteristics of the tip planforms, not to establish a direct relationship with the quantitative data discussed previously. However, the quantitative data presented in previous sections are used as a guide in the interpretation of the flow visualization photographs. All results presented in this section were acquired at a dynamic pressure of 10 psf, with a corresponding Reynolds number of 3.91×10^5.

Figures 17(a) and (b) illustrate the upper and lower surface flow patterns on the RC10/08 tip for $\alpha_T = -5.0°$ and $\Delta\theta = -13.0°$. The data plotted in figure 6(a) show that at $\alpha_T = -5.0°$ the tip is still generating positive lift, although at a slightly higher Reynolds number than for the present case. In the leading-edge region on both surfaces, the oil patterns confirm that the flow is still attached; however, most of the flow is characterized by the formation of river patterns. As explained in reference 7, this is caused by the excessive application of oil on the model surface. As seen in the photographs, the influence of pressure gradients and shear stresses that normally determine the surface oil pattern is completely overcome by the effect of gravity on the thick oil film.

For $\alpha_T = -3.0°$ (fig. 18), the direction of the flow changes by roughly 90° on the upper surface in the vicinity of the junction between the wing and the tip. The surface flow is drawn toward the low-pressure region caused by the presence of the wing vortex; at this condition, $\alpha_W = 10.0°$ and the wing loading is quite high. Clearly, the flow is still attached in this region. The change in direction of the surface flow is not observed on the lower surface (fig. 18(b)). As the wing angle of attack is increased at this constant value of $\Delta\theta$, portions of the tip upper-surface flow continue to be drawn toward the wing and remain attached. At $\alpha_T = -1.0°$ (fig. 19), despite the negative tip angle of attack, the loading is positive and moderately large ($C_{L_T} \approx 0.4$, see fig. 6(a)).

At $\alpha_T = 2.0°$ (fig. 20, $\alpha_W = 15.0°$), a sharp separation line with reattachment is defined along the swept portion of the upper-surface leading edge. The tip inboard-surface flow is still being drawn toward the wing/tip juncture and is attached. This is of particular significance since it indicates that despite strong interactions between tip vortex and wing vortex, the tip surface flow does not separate prematurely in this area. The character of the flow on the lower surface did not change appreciably throughout the angle-of-attack sweep.

The photographs for the RC10/05 tip surface at $\Delta\theta = -2.5°$ are shown in figures 21 through 24. At $\alpha_T = -2.5°$ (fig. 21), river patterns caused by excessive oil are observed, as before. As α_T is increased to 2.5° (fig. 22), a small region of separated flow develops on the upper surface close to the leading edge. Downstream of this area, the flow has reattached. The change in direction of the flow toward the wing/tip junction is also clearly discernable here. On the lower surface, the flow is attached and smooth well beyond the leading edge, but river patterns dominate the aft portion of the surface.

At $\alpha_T = 7.5°$ and 12.5° (figs. 23 and 24), the region of separated flow increases in size near the outboard end of the tip. This is an example of classic flow separation in the tip region of a swept surface. The accumulation of mass within the boundary layer, resulting from spanwise flow, alters the pressure gradient such that the flow initially separates in the outboard region. The lift curves shown in figures 13(a) and 14(a) corroborate the conclusion that the flow is separating at this condition. At

8

low Reynolds numbers, the plots show the onset of flow separation at about $\alpha_T = 8°$ to $9°$ for $\Delta\theta = -2.5°$.

Tip Aerodynamic Parameters

Tip Aerodynamic Center

The location of the tip aerodynamic center along the mean aerodynamic chord is an important design parameter for free-tip planforms. For a tip oscillating about a mean angle of attack, the frequency of damped free vibration is directly related to the magnitude of the tip aerodynamic spring effect. This magnitude primarily depends on the ability of the tip to generate a restoring moment about the pitch axis. Since the resultant lift acts at the aerodynamic center, favorable restoring moments are obtained for aft aerodynamic center locations.

The locations of the tip aerodynamic centers projected along the x axis of the wing-fixed coordinate system are calculated here from the data acquired for both tips. The goal is to determine whether $\Delta\theta$, which is a function of wing angle of attack (and thus is influenced by wing vortex strength), has any impact on tip aerodynamic-center location.

With the loads acting at the aerodynamic center, the tip pitching moment about an arbitrary point x along the wing chord may be expressed as

$$C_{m_T}\big|_x = C_{m_{ac}} + \left(C_{L_T} \cos \alpha_T\right)\left(\frac{x - x_{ac}}{c_T}\right) + \left(C_{D_T} \sin \alpha_T\right)\left(\frac{x - x_{ac}}{c_T}\right) \qquad (3)$$

where x is measured along the axis shown in figure 2, with the positive direction pointing aft. The parameter x_{ac}/c_T is the projection on this axis of the tip aerodynamic center location. If equation (3) is differentiated with respect to C_{L_T}, the term $dC_{m_{ac}}/dC_{L_T}$ drops out by definition of the aerodynamic center. Also, if α_T is assumed to be small and the contribution of the drag is neglected, the following expression is obtained:

$$\frac{dC_{m_T}\big|_x}{dC_{L_T}} = \frac{x - x_{ac}}{c_T} \qquad (4)$$

In the present study, since the tip pitching moment was measured by a balance located at the inboard wing quarter-chord point, the value $x/c_T = 0.0$ (see fig. 3) can be substituted into equation (4), and the aerodynamic-center location can be easily calculated once the slope $dC_{m_{0.0}}/dC_{L_T}$ is known. The slopes for different values of Re and $\Delta\theta$ were calculated by fitting first-order curves to the test results presented earlier; these slopes are listed in tables C3 and C6 of appendix C. Figure 25 shows the resulting locations of the aerodynamic center for the two tips, as a function of $\Delta\theta$. For both tips, the position of the aerodynamic center is relatively constant with $\Delta\theta$. For the RC10/08 tip, figure 25 shows variations with Reynolds number of up to 6% of the chord length.

9

Lift and Pitching Moment Data

The tip-planform lift and pitching moment slopes were computed from the complete body of experimental data and are listed in tables C1 to C6 in appendix C. A quick check of the results shows no variation with $\Delta\theta$ in the values of $\partial C_{L_T}/\partial\alpha_T$ and $\partial C_{m_T}/\partial\alpha_T$, for a fixed value of Reynolds number. This is expected, since these parameters are typically affected only by planform geometry and Mach number.

The y-intercepts for each curve are also listed in appendix C (tables C1 to C6). These are the

coefficients $C_{L_0} = C_{L_T}\big|_{\alpha_T=0°}$ and $C_{m_0} = C_{m_T}\big|_{\alpha_T=0°}$ and $C_{m_0} = C_{m_T}\big|_{C_{L_T}=0°}$. The first two

parameters are plotted in figure 26 for the RC10/08 tip. Generally, the value of C_{L_0} increases with negative $\Delta\theta$. This is due to the strength of the upwash, which increases with α_W. Figure 26(b) shows the associated effect on C_{m_0}, which increases negatively with negative $\Delta\theta$. This is due to the effect of increasing C_{L_0}, since it was shown above that the location of the tip aerodynamic center is essentially invariant with $\Delta\theta$.

Figure 27 shows the variation of C_{L_0} and C_{m_0} with $\Delta\theta$ for the RC10/05 tip. The same trends as were observed in figure 26 are seen here, but with more consistency. The data seem to suggest a linear variation of these parameters with $\Delta\theta$. The variations with Reynolds number are probably caused by boundary-layer thickness effects on chordwise pressure distributions. Figures 26 and 27 thus quantify the variation with α_W of the upwash on C_{L_T} and C_{m_T} caused by the strong influence of α_W on the $\Delta\theta$ parameter.

USE OF STEADY FLOW EXPERIMENTAL DATA FOR CALCULATION OF FREE-TIP MOTION

Experimental data such as those presented in this report can be used to bridge the gap between the cases of the deflected tip in steady flow and the free vibration in a free stream of an independently mounted tip surface pitching about the quarter-chord of the inboard wing. From an analytical standpoint, the free-oscillation case is a complex problem in which the governing equations of fluid dynamics must be solved simultaneously with the tip single-degree-of-freedom equation of motion. The equation of motion that appears in reference 8 for a two-dimensional rotary-wing aerodynamic environment is rewritten as follows for a tip mounted on a fixed wing of finite span:

$$I_\alpha \ddot{\alpha}_T + K_s\left(\alpha_T - \theta_p\right) = C_{m_T}\left(\frac{1}{2}\rho V_\infty^2\right)S_T c_T \tag{5}$$

This formulation applies only to a tip surface oscillating about an axis along the chord of a rigid wing, with α_W fixed. The term on the right-hand side is the aerodynamic moment and includes aerodynamic spring and damping effects. The evaluation of C_{m_T} is the primary subject of this section.

10

The results presented in the current report focus on the variation of aerodynamic loads as a function of $\Delta\theta$. Although important information can be derived from data in this form, a different approach can be developed in which the parameters appearing in the expression for $\Delta\theta$ are considered independently, along with time-dependent variables. For the case of general unsteady motion of the tip surface with zero yaw (with α_W assumed fixed), the tip pitching-moment coefficient, varying as a function of time, can be written as

$$C_{m_T} = C_{m_T}\left[\alpha_W, \alpha_T(t), \dot{h}_T(t), q_T(t)\right] \tag{6}$$

For the case of arbitrary motion, two rigid-body degrees of freedom have been included: (1) wing plunging motion, which produces the $\dot{h}_T(t)$ term, and (2) the tip pitch rate, $q_T(t)$, which accounts for the time rate of change of tip incidence angle relative to a horizontal reference plane. A Taylor series expansion of C_{m_T} about the point where $\alpha_W = \alpha_T = \dot{h}_T = q_T = 0$ can be written as follows:

$$C_{m_T}(\alpha_W, t) = C_{m_0} + \left(\partial C_{m_T}/\partial \alpha_W\right)\alpha_W + \left(\partial C_{m_T}/\partial \alpha_T\right)\alpha_T$$

$$+ \left[\partial C_{m_T}/\partial\left(\dot{h}_T/V_\infty\right)\right]\left(\dot{h}_T/V_\infty\right) + \left[\partial C_{m_T}/\partial\left(q_T c_T/V_\infty\right)\right]\left(q_T c_T/V_\infty\right) \tag{7}$$

This expansion is linearized by neglecting second- and higher-order terms, since the angles and rates are assumed to be small. The partial derivatives are evaluated at the point about which the series is expanded. The second and third terms in the series will be discussed first.

Equation (7) cannot be used with data acquired in terms of $\Delta\theta$, since $\partial/\partial(\Delta\theta)$ terms (in an expansion with $\Delta\theta$ as the independent variable) imply a variation of both α_W and α_T simultaneously, thus violating the definition of the partial derivative. To determine the first two slopes of the Taylor series expansion, the data would have to be acquired in a different manner; instead of varying the angle of incidence of the entire configuration with the tip deflected at a fixed angle relative to the wing ($\Delta\theta$), the measurements would have to be taken at fixed values of α_W while the tip angle of attack was varied. Thus, families of curves of C_{m_T} vs α_T would be obtained for constant values of α_W. The derivative $\partial C_{m_T}/\partial \alpha_W$ would then easily be obtained by measuring the change in C_{m_T} among the different curves, for $\alpha_T = 0.0°$. The second partial derivative is simply the slope $\partial C_{m_T}/\partial \alpha_T$ of the tip pitching moment coefficient curve for $\alpha_W = 0.0°$. Unfortunately, this approach was not implemented for the present study because the test focused on deflected tips, for which data have traditionally been presented as a function of $\Delta\theta$ (refs. 1–5).

The last two terms in the series expansion (eq. (7)) follow from a quasi-steady formulation in which $C_{m_T}(\alpha_W, t)$ depends on the instantaneous values of $\dot{h}_T(t)$ and $q_T(t)$. One problem with this approach is that it is based on the assumption that $\partial C_{m_T}/\partial\left(\dot{h}_T V_\infty\right)$ and $\partial C_{m_T}/\partial\left(q_T c_T/V_\infty\right)$ are constant and can be evaluated or measured experimentally. A more serious problem with equation (7) is that it does not acknowledge any effects that the past history of the motion may have on the instantaneous aerodynamic response.

Following the methods of indicial unsteady aerodynamic theory presented in reference 9, the pitching moment coefficient may be formulated to include the effects of previous motion on the current loading, as follows:

$$C_{m_T}(\alpha_W, t) = C_{m_0} + \left(\partial C_{m_T}/\partial \alpha_W\right)\alpha_W + \int_0^t C_{m_\alpha}[t - \tau; \alpha_T(\tau), q_T(\tau)] \frac{d\alpha_T(\tau)}{d\tau} d\tau$$

$$+ \frac{c_T}{V_\infty} \int_0^t C_{m_q}[t - \tau; \alpha_T(\tau), q_T(\tau)] \frac{dq_T(\tau)}{d\tau} d\tau \qquad (8)$$

The first parameter in the integrands represents the incremental pitching moment response at time t that corresponds to a unit step change in α_T and q_T that occurs at time τ. If $\alpha_T(\tau)$ and $q_T(\tau)$ are approximated by a superposition of unit step changes, then the pitching moment response is simply the summation of incremental responses to unit step changes in $\alpha_T(\tau)$ and $q_T(\tau)$. Equation (8) has already been simplified in that $C_{m_\alpha}[...]$ and $C_{m_q}[...]$ are based only on the values of α_T and q_T at the origin of the step. In principle, the responses should be based on the complete histories of α_T and q_T. The histories could be reconstructed by Taylor series expansions about the time of the step initiation (for example, $\alpha_T(t') \approx \alpha_T(\tau) - \dot{\alpha}_T(\tau)(\tau - t') - ...$, where t' represents a time earlier than τ); however, as explained in reference 9, the indicial responses should have "forgotten" long-past events. Also, limiting the present analysis to that of slowly varying motions allows for the exclusion of $\dot{\alpha}_T$ and $\dot{q}_T$ terms.

A final assumption is required before a working form of equation (8) can be obtained. If $\alpha_T(t)$ and $\theta_T(t)$ are represented as harmonic functions, powers of $q_T(t)$ higher than the first will be of second and higher orders in frequency $[q_T(t) = \dot{\theta}_T(t)]$ After expressing the integrands of equation (8) in terms of deficiency functions and expanding these in Taylor series about $q_T(0) = 0$, we may neglect all terms containing powers of $q_T(t)$ higher than the first, since the frequency is assumed to be small.

The expression that results from integrating equation (8) contains the term $C_{m_T}[\infty; \alpha_T(t), 0]$ described in reference 9 as the pitching moment coefficient measured in a steady flow with α_W fixed, at the instantaneous value $\alpha_T(t) = 0$ and $q_T(t) = 0$. The appearance of this term is the key to the use of experimental data in the computation of free-tip oscillatory motion. In the context of the rigid semispan wing with free-pitching tip, this term takes the following form:

$$C_{m_T}[\infty; \alpha_T(t), 0] = C_{m_0} + \left(\partial C_{m_T}/\partial \alpha_W\right)\alpha_W + \left(\partial C_{m_T}/\partial \alpha_T\right)\alpha_T(t) \qquad (9)$$

The first three coefficients are parameters that can be evaluated experimentally, as discussed previously. The integrated version of equation (8) can be further simplified by the substitution $\dot{\alpha}_T = q_T$, which holds for rectilinear motion in the present configuration.

Substituting equation (9) into the simplified version of equation (8) leads to the final working form, which can be used for free-tip analysis and is given by

$$C_{m_T}(\alpha_W, t) = C_{m_0} + \left(\partial C_{m_T}/\partial \alpha_W\right)\alpha_W + \left(\partial C_{m_T}/\partial \alpha_T\right)\alpha_T(t) + \left\{C_{m_{\dot\alpha}}[\alpha_T(t)]\right\}\frac{\dot\alpha_T(t)c_T}{V_\infty} \quad (10)$$

The last term is analogous to the pitch-damping stability derivative. In this case however, it must be evaluated or measured for each value of $\alpha_T(t)$ within the expected range of the oscillatory motion. This may be done by prescribing a small-amplitude harmonic oscillation using each expected value of $\alpha_T(t)$ as a mean. The required data can be obtained from experimental measurements or by solving numerically the appropriate unsteady field equations of fluid mechanics, for pure harmonic pitching motion. For a more comprehensive data base of coefficients $C_{m_{\dot\alpha}}[\alpha_T(t)]$, the prescribed motion can be repeated for several frequencies. The most efficient and cost-effective approach to achieve this for the free-tip on a semispan wing would be to use a panel-method computer code for unsteady motion, such as the one described in reference 10. The coefficient is evaluated from the component of the pitching-moment-response time history that is 90° out of phase with the prescribed angle of attack. This approach was used successfully in reference 11 for the case of an oscillating flap on an airfoil in transonic flow. For that study, the time-dependent Euler equations were solved to obtain the desired coefficients.

The advantage of this approach is obvious. Once the coefficients for a given tip configuration have been tabulated or curve-fitted, the oscillatory motion of a free-pitching tip may be calculated from equation (5) by a simple numerical integration scheme, and by obtaining $C_{m_T}(\alpha_W, t)$ from equation (10) with current values of $\alpha_T(t)$ and $\dot\alpha_T(t)$. Hence, the mechanical characteristics of the tip (I_α, K_s) can be altered and the tip motion recomputed as long as the expected response frequency is within the range of prescribed-motion frequencies used to evaluate $C_{m_{\dot\alpha}}[\alpha_T(t)]$.

The preceding discussion provides a framework for future research in the analysis of free-pitching tip motion. The relationship between the evaluation or measurement of steady aerodynamic loads and the solution of the unsteady tip-motion problem has been clearly established.

CONCLUDING REMARKS

The aerodynamic characteristics of two new tip surfaces proposed for a small-scale Free-Tip Rotor model were measured at dynamic pressures from 5 to 25 psf and Reynolds numbers from 2.76×10^5 to 6.18×10^5. The tips had similar planform characteristics, but different airfoil distributions, varying from thickness ratios of 10% on the inboard portion to 8% or 5% toward the outboard edge of the tip. The major issues addressed in this study are as follows:

1. Lift and pitching moment data support the theory that upwash from the semispan wing has a strong influence on the aerodynamic loading of the deflected tip. This effect is proportional to the wing angle of attack.

2. The upwash from the inboard wing reduces the stall angle of the tip surface, especially at lower Reynolds numbers. A slight increase in Reynolds number is sufficient to delay this effect.

13

3. Experimental evidence suggests that the reduction in tip induced drag associated with the wing upwash reduces the total tip drag. However, there is apparently a negative value of $\Delta\theta$ for which the drag reduction reaches its limit.

4. The flow visualization results show no outstanding features that might be detrimental to the performance of the tips. As the lift coefficient is increased, the flow separates gradually on the outboard portion of the tip. Surface flows on the inboard portion of the tip are drawn toward the gap between the wing and the tip, but remain attached up to the inboard side edge of the surface.

5. Lift and pitching-moment slopes, as well as coefficients for zero angle of attack, have been computed for both tips. The test results indicate that the surface aerodynamic centers are sufficiently aft of the quarter-chord pitch axis to be suitable for free-tip designs. The variations in aerodynamic center position of the tip are minimal and are not believed to be due to changes in wing loading.

6. A new approach that treats wing and tip angles of attack as independent parameters was proposed. The required Taylor series coefficients can be easily obtained from test results by graphical means. These can, in turn, be combined with tabulated values of tip pitch-damping coefficients to obtain the time-varying pitching moment response of a free-tip. This method allows the calculation of general unsteady tip motion without repeatedly solving the coupled single-degree-of-freedom/ aerodynamic problem.

APPENDIX A

AIRFOIL SURFACE ORDINATES AND WING TWIST DISTRIBUTION

This appendix contains the following tables and figures:

Table A1. Surface coordinates for the RC05 airfoil section.

Table A2. Surface coordinates for the RC08 airfoil section.

Table A3. Surface coordinates for the RC10 airfoil section.

Table A4. Surface coordinates for the V23010 airfoil section.

Figure A1. Semispan wing-twist distribution.

Table A1. Surface coordinates for the RC05 airfoil section

x/c[*]	z_u/c[**]	z_l/c[†]	x/c[*]	z_u/c[**]	z_l/c[†]
0.000000	0.000000	0.000000	0.444581	0.027785	−0.022323
0.001007	0.003369	−0.002282	0.476209	0.027498	−0.022286
0.004023	0.006872	−0.004436	0.507933	0.027046	−0.022115
0.009036	0.010424	−0.006447	0.539625	0.026399	−0.021793
0.016026	0.013926	−0.008314	0.571157	0.025542	−0.021316
0.024964	0.017264	−0.010033	0.602403	0.024481	−0.020683
0.030154	0.018834	−0.010844	0.633237	0.023223	−0.019893
0.041946	0.021703	−0.012369	0.663534	0.021805	−0.018951
0.063075	0.025143	−0.014439	0.707707	0.019486	−0.017251
0.071008	0.026028	−0.015074	0.736136	0.017902	−0.015931
0.088162	0.027389	−0.016253	0.750000	0.017120	−0.015216
0.097365	0.027870	−0.016797	0.763613	0.016350	−0.014471
0.116978	0.028482	−0.017791	0.790028	0.014850	−0.012895
0.138133	0.028707	−0.018650	0.827430	0.012667	−0.010414
0.160745	0.028667	−0.019374	0.850737	0.011192	−0.008760
0.172570	0.028586	−0.019687	0.872632	0.009658	−0.007178
0.197195	0.028371	−0.020221	0.902635	0.007258	−0.005058
0.236387	0.028062	−0.020833	0.928992	0.004954	−0.003354
0.250000	0.027990	−0.020997	0.951463	0.003090	−0.002104
0.277967	0.027907	−0.021289	0.975036	0.001695	−0.001079
0.292293	0.027892	−0.021422	0.983974	0.001472	−0.000784
0.321557	0.027905	−0.021671	0.995977	0.001658	−0.000515
0.351540	0.027946	−0.021900	0.997736	0.001756	−0.000506
0.382121	0.027967	−0.022102	0.999748	0.001897	−0.000547
0.413176	0.027928	−0.022252	1.000000	0.001900	−0.000600

[*]x/c is the chordwise airfoil station for surface definition.

[**]z_u/c is the airfoil upper-surface ordinate.

[†]z_l/c is the airfoil lower-surface ordinate.

Table A2. Surface coordinates for the RC08 airfoil section

x/c*	z_u/c**	z_l/c †
0.000000	0.000000	0.000000
0.003140	0.006710	-0.006560
0.011700	0.013120	-0.010960
0.025340	0.019000	-0.014450
0.043690	0.024550	-0.017290
0.065080	0.029520	-0.019510
0.088890	0.033890	-0.021290
0.114710	0.037700	-0.022780
0.142390	0.040960	-0.024030
0.171860	0.043760	-0.025130
0.202980	0.046060	-0.026090
0.235600	0.047890	-0.026930
0.269590	0.049280	-0.027910
0.304840	0.050230	-0.028530
0.341210	0.050750	-0.028770
0.378400	0.050870	-0.029130
0.416120	0.050570	-0.029340
0.454040	0.049860	-0.029390
0.491990	0.048760	-0.029290
0.529830	0.047250	-0.029020
0.567660	0.045330	-0.028580
0.605530	0.043000	-0.027960
0.643670	0.040240	-0.027130
0.682380	0.037040	-0.026050
0.721500	0.033420	-0.024690
0.760570	0.029440	-0.023000
0.798420	0.025280	-0.020990
0.834570	0.021070	-0.018670
0.869270	0.016860	-0.015990
0.902800	0.012710	-0.012930
0.935430	0.008640	-0.009420
0.967820	0.004900	-0.005130
1.000000	0.001300	-0.000500

*x/c   is the chordwise airfoil station for surface definition.

**z_u/c is the airfoil upper-surface ordinate.

†z_l/c is the airfoil lower-surface ordinate.

Table A3. Surface coordinates for the RC10 airfoil section

x/c*	z_u/c**	z_l/c†
0.000000	0.000000	0.000000
0.003100	0.009060	-0.007650
0.010930	0.017000	-0.012300
0.024030	0.024620	-0.016190
0.042140	0.031930	-0.019500
0.063470	0.038540	-0.022030
0.087240	0.044350	-0.024000
0.113050	0.049440	-0.025610
0.140750	0.053760	-0.026960
0.170230	0.057480	-0.028170
0.201370	0.060510	-0.029230
0.234020	0.062920	-0.030200
0.268070	0.064740	-0.031070
0.303430	0.065960	-0.031840
0.339950	0.066610	-0.032490
0.377330	0.066720	-0.033010
0.415240	0.066270	-0.033370
0.453360	0.065280	-0.033570
0.491480	0.063760	-0.033600
0.529490	0.061700	-0.033460
0.567460	0.059090	-0.033130
0.605470	0.055930	-0.032600
0.643780	0.052200	-0.031840
0.682760	0.047870	-0.030790
0.722320	0.042960	-0.029390
0.761850	0.037580	-0.027580
0.800020	0.032000	-0.025360
0.836230	0.026440	-0.022720
0.870820	0.020960	-0.019590
0.904090	0.015640	-0.015940
0.936310	0.010520	-0.011710
0.968280	0.006000	-0.006330
1.000000	0.001800	-0.000200

*x/c is the chordwise airfoil station for surface definition.

**z_u/c is the airfoil upper-surface ordinate.

†z_l/c is the airfoil lower-surface ordinate.

Table A4. Surface coordinates for the V23010 airfoil section

x/c*	z_u/c**	z_l/c†
0.00000	–0.02250	–0.02250
0.00500	–0.00780	–0.03290
0.01000	–0.00240	–0.03620
0.01500	0.00190	–0.03780
0.02500	0.00960	–0.03940
0.03500	0.01550	–0.04040
0.04700	0.02140	–0.04120
0.06000	0.02650	–0.04200
0.08000	0.03270	–0.04340
0.11000	0.03960	–0.04490
0.15000	0.04550	–0.04710
0.19000	0.04890	–0.04940
0.23000	0.04990	–0.05130
0.27000	0.04990	–0.05220
0.31000	0.04970	–0.05215
0.35000	0.04900	–0.05170
0.39000	0.04800	–0.05050
0.43000	0.04650	–0.04870
0.47000	0.04460	–0.04680
0.51000	0.04240	–0.04400
0.55000	0.03970	–0.04120
0.59000	0.03690	–0.03800
0.63000	0.03360	–0.03460
0.67000	0.03010	–0.03080
0.71000	0.02630	–0.02690
0.75000	0.02230	–0.02260
0.79000	0.01810	–0.01820
0.83000	0.01370	–0.01360
0.87000	0.00930	–0.00930
0.91000	0.00560	–0.00570
0.94500	0.00280	–0.00310
0.96000	0.00235	–0.00235
1.00000	0.00235	–0.00235

*x/c is the chordwise airfoil station for surface definition.

**z_u/c is the airfoil upper-surface ordinate.

†z_l/c is the airfoil lower-surface ordinate.
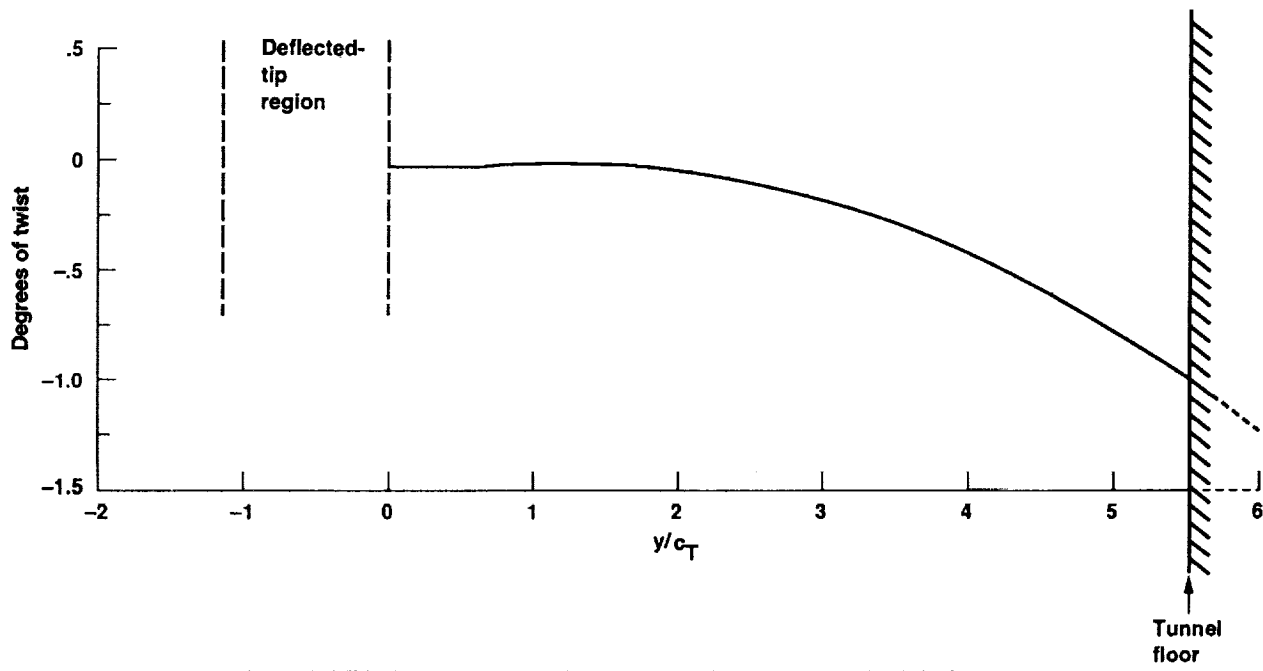
Figure A1. Semispan wing-twist distribution.

APPENDIX B

WIND TUNNEL CORRECTIONS

Standard wind tunnel wall corrections were applied in accordance with the methods outlined in reference 12. As recommended by the authors for such cases, the semispan wing was modeled as a full-span surface with twice the length of the half-span surface. The fictitious wind tunnel was also assumed to have a ratio of breadth over height (B/H) of 14 ft/10 ft = 1.40. The following is a summary of these corrections:

Velocity Correction for Solid-Body Blockage and Wake Blockage

The total velocity increment is

$$\varepsilon = \varepsilon_{sb} + \varepsilon_{wb}$$

where

ε_{sb} = f (wing volume, tunnel area, model span, t/c, B/H)

ε_{wb} = f (wing area, tunnel area, wing drag coefficient)

Since wing loads were not measured, an empirical estimate of wing drag was used.

The corrected velocity is

$$V_\infty = V_u(1 + \varepsilon)$$

the corrected Reynolds number is

$$Re = Re_u(1 + \varepsilon)$$

and the corrected dynamic pressure is

$$q = q_u(1 + 2\varepsilon)$$

where the subscript u refers to the uncorrected value of the parameter. For this test, $\varepsilon = 3.01 \times 10^{-4}$ was computed.

Corrections for Downwash and Streamline Curvature

During the data reduction process, corrections were applied to the following tip load parameters in the given order:

The first correction was

$$C_L = C_{L_u}(1 - 2\varepsilon) + (\Delta C_L)_{sc}$$

where

$$(\Delta C_L) = -C_{L_\alpha}(\Delta\alpha)_{sc}$$

$$(\Delta\alpha)_{sc} = t_2(\Delta\alpha)_{dw}$$

$$t_2 = f \text{ (chord length, H/B, B)}$$

$$(\Delta\alpha)_{dw} = f \text{ } (C_{L_u}, \text{ equivalent vortex span, tunnel area, tip planform area, model chord length)}$$

For this test, the computed correction parameters yield

$$C_L = C_{L_u}(1 - 2\varepsilon) - (5.54 \times 10^{-5})C_{L_u}$$

The second correction was

$$\alpha_T = \alpha_{T_u} + (\Delta\alpha)_{dw}(1 + t_2)$$

Therefore,

$$\alpha_T = \alpha_{T_u} + 0.0373C_{L_u}(1 + 0.033)$$

The third correction was

$$C_D = C_{D_u}(1 - 2\varepsilon) + \Delta C_D$$

where

$$\Delta C_D = f \text{ } (C_L, \text{ vortex span, tunnel area, tip planform area, model chord length)}$$

22

Therefore,

$$C_D = C_{D_u}(1 - 2\varepsilon) + (6.51 \times 10^{-4})C_L^2$$

The fourth correction was

$$C_m = C_{m_u}(1 - 2\varepsilon) - 0.25(\Delta C_L)_{sc}$$

Therefore,

$$C_m = C_{m_u}(1 - 2\varepsilon) - 0.25(-5.54 \times 10^{-5})C_{L_u}$$
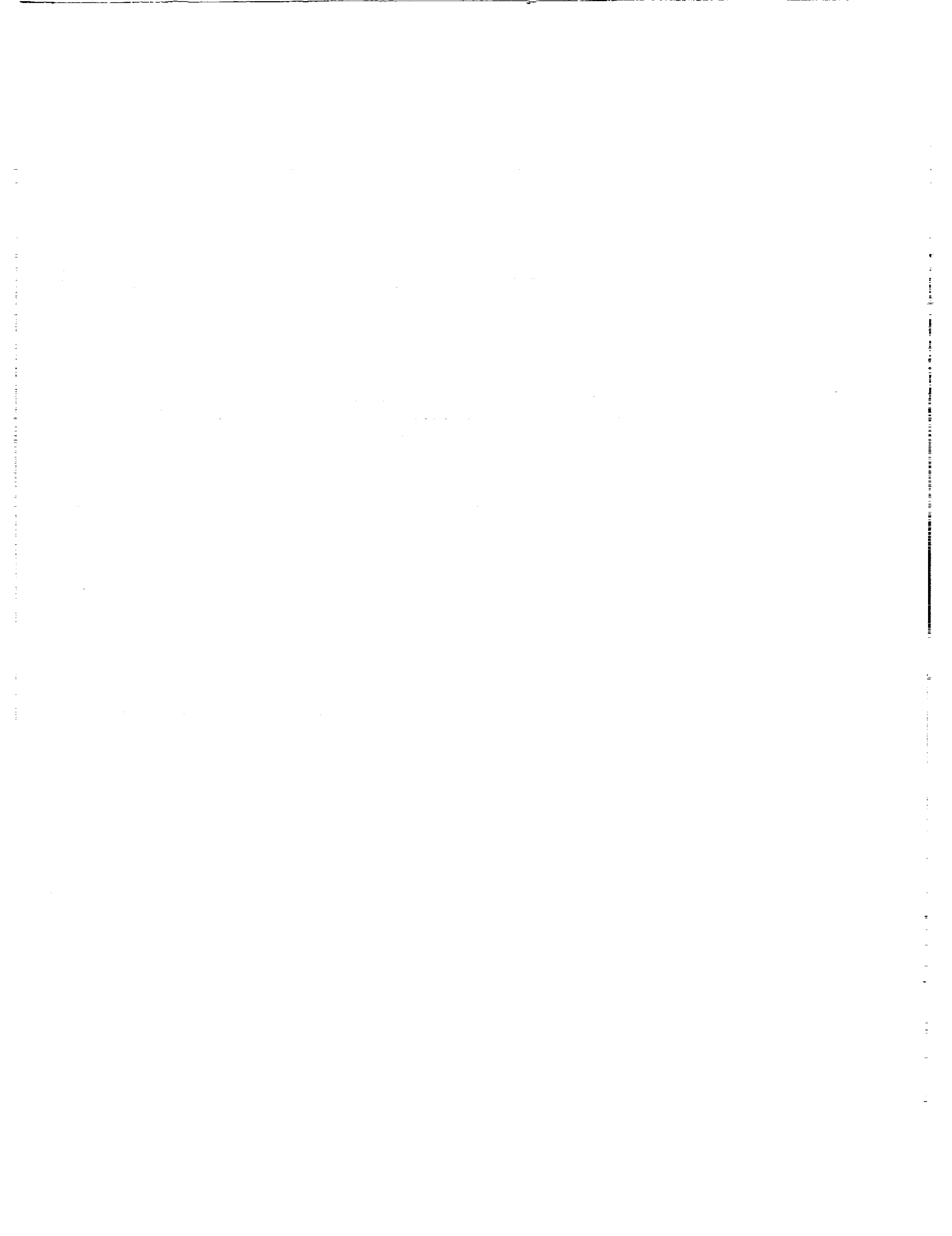
APPENDIX C

TIP AERODYNAMIC PARAMETERS

This appendix contains the following tables:

Table C1. Lift-curve slopes and zero-alpha lift coefficients for the RC10/08 tip.

Table C2. Pitching-moment-curve slopes and zero-alpha pitching moment coefficients for the RC10/08 tip.

Table C3. Pitching-moment-curve slopes and zero-lift pitching moment coefficients for the RC10/08 tip.

Table C4. Lift-curve slopes and zero-alpha lift coefficients for the RC10/05 tip.

Table C5. Pitching-moment-curve slopes and zero-alpha pitching moment coefficients for the RC10/05 tip.

Table C6. Pitching-moment-curve slopes and zero-lift pitching moment coefficients for the RC10/05 tip.

Table C1. Lift-curve slopes and zero-alpha lift coefficients for the RC10/08 tip

Re	$\Delta\theta$ (deg)	C_{L_α} (deg^{-1})	C_{L_0}
2.76×10^5	−9.0	0.0735	0.6308
	−3.5	0.0758	0.0865
	−3.5	0.0696	0.1100
	1.5	0.0765	0.1601
3.91×10^5	−13.0	0.0848	0.5067
	−9.0	0.0928	0.6214
	−3.5	0.0808	0.1060
	−3.5	0.0738	0.1055
	1.5	0.0805	0.0814
4.79×10^5	−13.0	0.0845	0.5031
	−9.0	0.0847	0.4469
	−3.5	0.0860	0.1214
	−3.5	0.0809	0.1142
	1.5	0.0845	0.0165
5.53×10^5	−13.0	0.0875	0.5000
	−9.0	0.0866	0.4531
	−3.5	0.0822	0.1338
	1.5	0.0774	0.0275
6.18×10^5	−13.0	0.0797	0.4733
	−3.5	0.0805	0.1302

Table C2. Pitching-moment-curve slopes and zero-alpha pitching moment coefficients for the RC10/08 tip

Re	$\Delta\theta$ (deg)	C_{m_α} (deg^{-1})	C_{m_0}
2.76×10^5	−13.0	−0.0216	−0.1349
	−9.0	−0.0158	−0.1225
	−3.5	−0.0197	−0.0457
	−3.5	−0.0198	−0.0525
	1.5	−0.0175	−0.0536
3.91×10^5	−13.0	−0.0167	−0.1254
	−9.0	−0.0172	−0.1139
	−3.5	−0.0191	−0.0468
	−3.5	−0.0187	−0.0542
	1.5	−0.0161	−0.0521
4.79×10^5	−13.0	−0.0230	−0.1314
	−9.0	−0.0212	−0.1128
	−3.5	−0.0222	−0.0443
	1.5	−0.0192	−0.0319
5.53×10^5	−13.0	−0.0242	−0.1308
	−3.5	−0.0218	−0.0444
	1.5	−0.0196	−0.0277
6.18×10^5	−13.0	−0.0219	−0.1223
	−9.0	−0.0238	−0.1151
	−3.5	−0.0215	−0.0422

Table C3. Pitching-moment-curve slopes and zero-lift pitching moment coefficients for the RC10/08 tip

Re	$\Delta\theta$ (deg)	dC_{m_T}/dC_{L_T} (deg^{-1})	C_{m_0}
2.76×10^5	−13.0	−0.2529	−0.0074
	−9.0	−0.2090	−0.0091
	−3.5	−0.2410	−0.0270
	−3.5	−0.2624	−0.0261
	1.5	−0.2193	−0.0242
3.91×10^5	−13.0	−0.2382	−0.0102
	−9.0	−0.1865	0.0021
	−3.5	−0.2373	−0.0214
	−3.5	−0.2539	−0.0273
	1.5	−0.2122	−0.0298
4.79×10^5	−13.0	−0.2738	0.0062
	−9.0	−0.2437	−0.0044
	−3.5	−0.2585	−0.0129
	−3.5	−0.2828	−0.0196
	1.5	−0.2266	−0.0283
5.53×10^5	−13.0	−0.2771	0.0076
	−9.0	−0.2681	0.0070
	−3.5	−0.2653	−0.0088
	1.5	−0.2526	−0.0208
6.18×10^5	−13.0	−0.2740	0.0074
	−9.0	−0.2435	0.0131
	−3.5	−0.2672	−0.0074

Table C4. Lift-curve slopes and zero-alpha lift coefficients for the RC10/05 tip

Re	$\Delta\theta$ (deg)	C_{L_α} (deg^{-1})	C_{L_0}
2.76×10^5	−10.0	0.0687	0.4344
	−8.0	0.0600	0.3449
	−2.5	0.0763	0.0901
3.91×10^5	−10.0	0.0792	0.4205
	−8.0	0.0788	0.2841
	−2.5	0.0855	0.0957
4.79×10^5	−10.0	0.0808	0.4043
	−8.0	0.0802	0.2982
	−2.5	0.0832	0.1747
5.53×10^5	−10.0	0.0804	0.3936
	−8.0	0.0807	0.2914
	−2.5	0.0793	0.1616
6.18×10^5	−10.0	0.0848	0.3955
	−2.5	0.0760	0.1498

Table C5. Pitching-moment-curve slopes and zero-alpha pitching moment coefficients for the RC10/05 tip

Re	$\Delta\theta$ (deg)	C_{m_α} (deg^{-1})	C_{m_0}
2.76×10^5	−10.0	−0.0153	−0.1002
	−8.0	−0.0141	−0.0797
	−2.5	−0.0172	−0.0331
3.9×10^5	−10.0	−0.0150	−0.0922
	−10.0	−0.0151	−0.0877
	−8.0	−0.0155	−0.0742
	−2.5	−0.0163	−0.0346
4.79×10^5	−10.0	−0.0163	−0.0831
	−10.0	−0.0153	−0.0852
	−8.0	−0.0163	−0.0719
	−2.5	−0.0171	−0.0340
5.53×10^5	−10.0	−0.0159	−0.0779
	−10.0	−0.0155	−0.0842
	−8.0	−0.0159	−0.0675
	−2.5	−0.0166	−0.0313
6.18×10^5	−10.0	−0.0164	−0.0753
	−10.0	−0.0159	−0.0828
	−2.5	−0.0163	−0.0288

Table C6. Pitching-moment-curve slopes and zero-lift pitching moment coefficients for the RC10/05 tip

Re	$\Delta\theta$ (deg)	dC_{m_T}/dC_{L_T} (deg^{-1})	C_{m_0}
2.76×10^5	−10.0	−0.2206	−0.0043
	−8.0	−0.2369	0.0017
	−2.5	−0.2098	−0.0169
3.9×10^5	−10.0	−0.2025	−0.0075
	−10.0	−0.2017	0.0015
	−8.0	−0.2028	−0.0164
	−2.5	−0.2088	−0.0118
4.79×10^5	−10.0	−0.2020	−0.0014
	−10.0	−0.1959	0.0073
	−8.0	−0.2030	−0.0114
	−2.5	−0.2047	0.0017
5.53×10^5	−10.0	−0.1981	0.0001
	−10.0	−0.1761	0.0065
	−8.0	−0.1967	−0.0102
	−2.5	−0.2094	0.0026
6.18×10^5	−10.0	−0.1930	0.0010
	−10.0	−0.1934	0.0249
	−2.5	−0.2141	0.0033
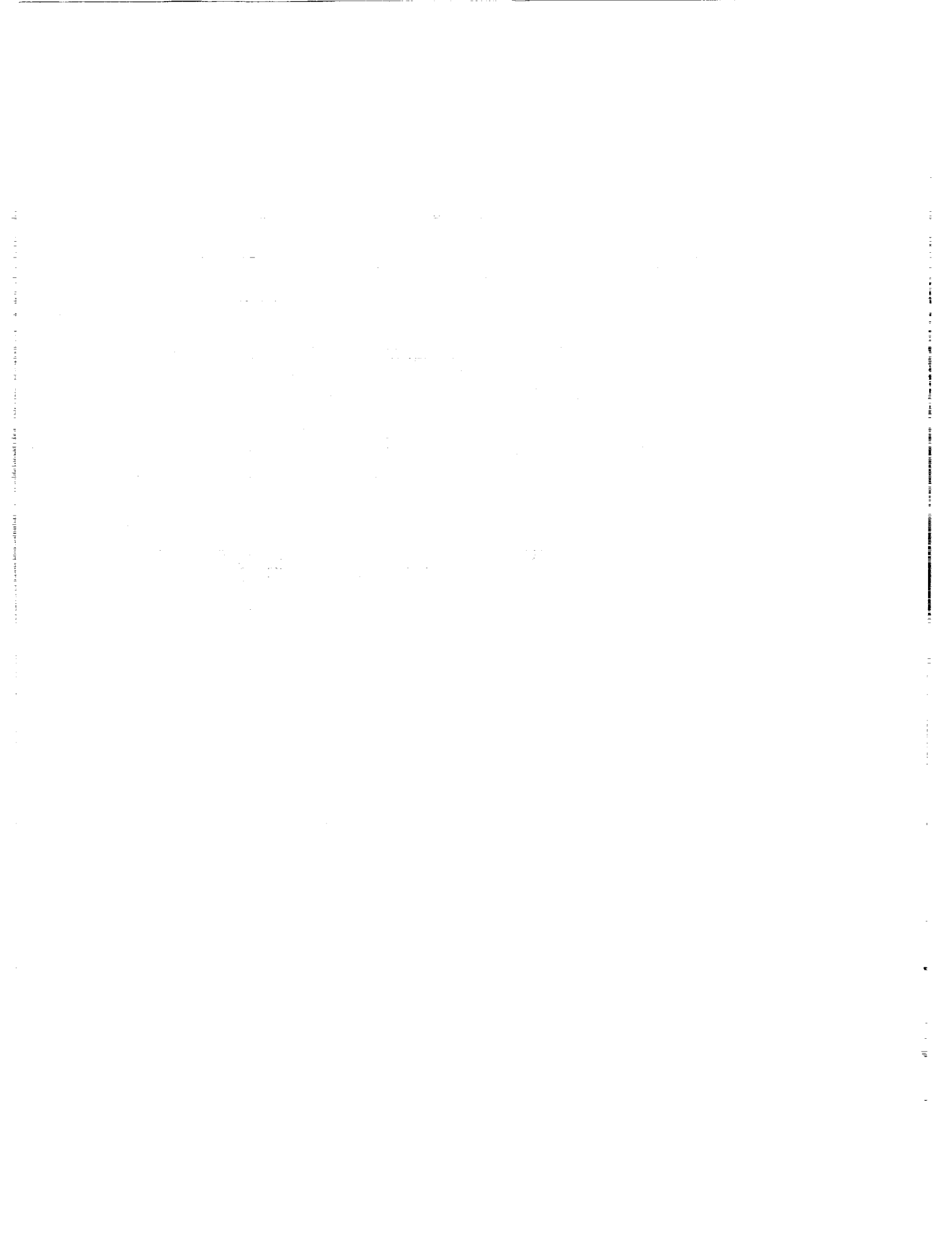
REFERENCES

1. Stroub, R. H.; Young, L. A.; Keys, C. N.; and Cawthorne M. H.: Free-Tip Rotor Wind Tunnel Test Results. AHS J., vol. 31, no. 3, July 1986, pp. 19-26.

2. Van Aken, J. M.: An Investigation of Tip Planform Influence on the Aerodynamic Load Characteristics of a Semispan Wing and Wing Tip. Report 5171-1, The University of Kansas Center for Research, Inc., Lawrence, KS, Dec. 1985.

3. Van Aken, J. M.; and Stroub, R. H.: Tip Aerodynamics from Wind Tunnel Test of Semispan Wing. NASA TM-88253, 1986.

4. Van Aken, J. M.: Experimental Investigation of the Influence of Tip Planform and Wing Sweep on the Tip Aerodynamic Load Characteristics. Report 7440-4, The University of Kansas Center for Research, Inc., Lawrence, KS, Nov. 1988.

5. Martin, D. M.; and Fortin P. E.: VSAERO Analysis of Tip Planforms for the Free-Tip Rotor. NASA CR-177487, 1988.

6. Schlichting, H.: Boundary Layer Theory. McGraw-Hill, New York, 1968.

7. Maltby, R. L.: Flow Visualization in Wind Tunnels Using Indicators. AGARDograph 70, Apr. 1962.

8. Yates, L.; and Kumagai, H.: Application of Two-Dimensional Unsteady Aerodynamics to a Free-Tip Rotor Response Analysis. NASA CR-177348, 1985.

9. Tobak, M.; and Schiff, L. B.: Aerodynamic Mathematical Modeling—Basic Concepts. AGARD Lecture Series on Dynamic Stability Parameters. AGARD-LS-114, May 1981.

10. Katz, J.; and Maskew, B.: Unsteady Low-speed Aerodynamic Model for Complete Aircraft Configurations. J. Aircraft, vol. 24, Apr. 1988.

11. Chyu, W. J.; and Schiff, L. B.: Nonlinear Aerodynamic Modeling of Flap Oscillations in Transonic Flow: A Numerical Validation. AIAA J., vol. 21, no. 1, Jan. 1983.

12. Pope, A.; and Harper, J.: Low-Speed Wind Tunnel Testing. Wiley, New York, 1966.
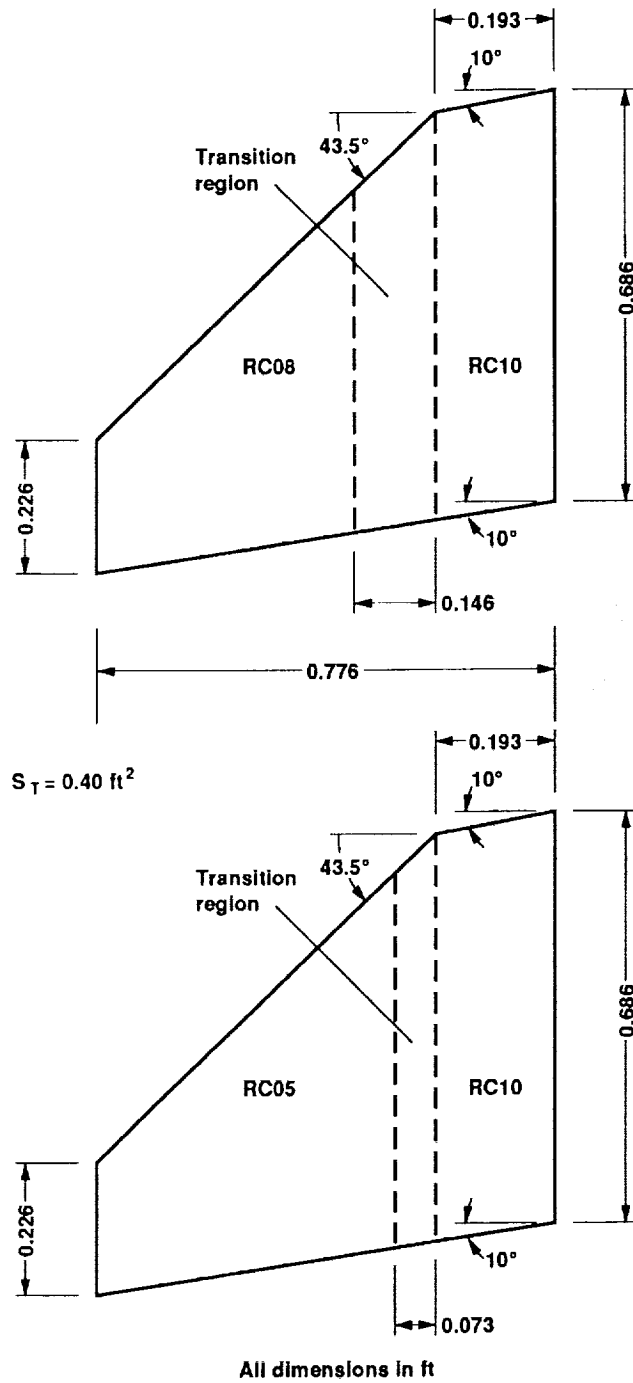
Figure 1. Geometry of tip planforms.
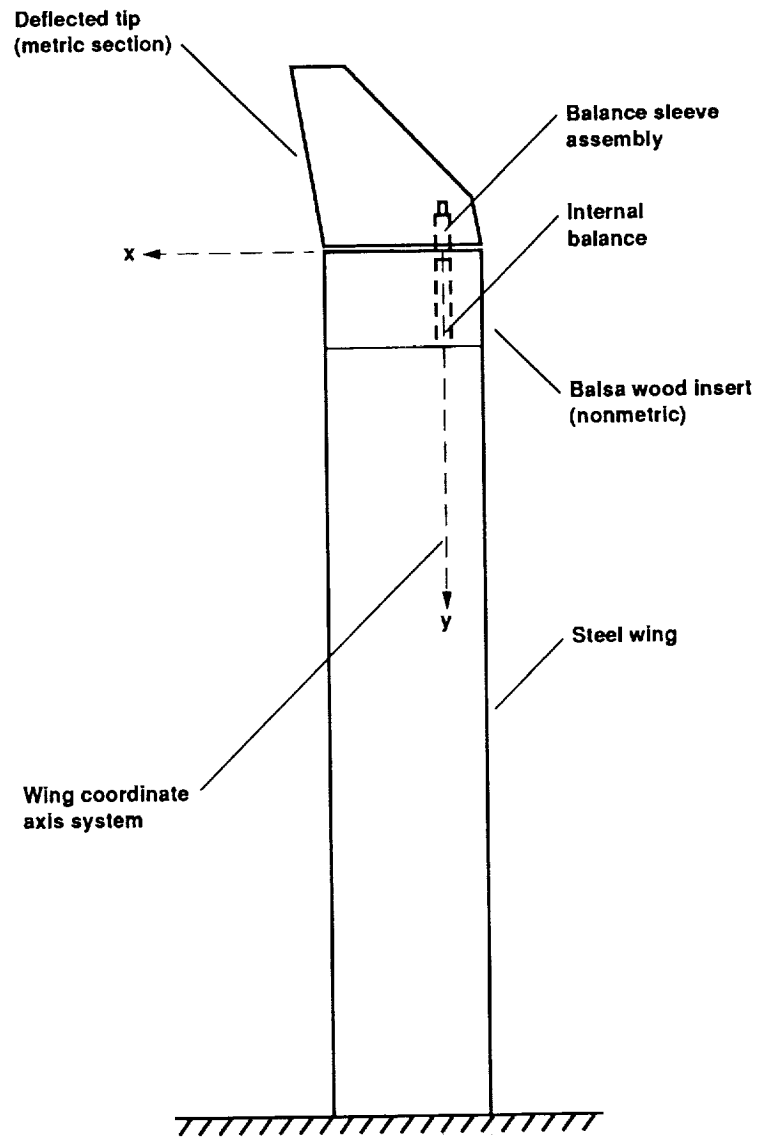
Figure 2. Wing and tip layout with wing-fixed axis system.
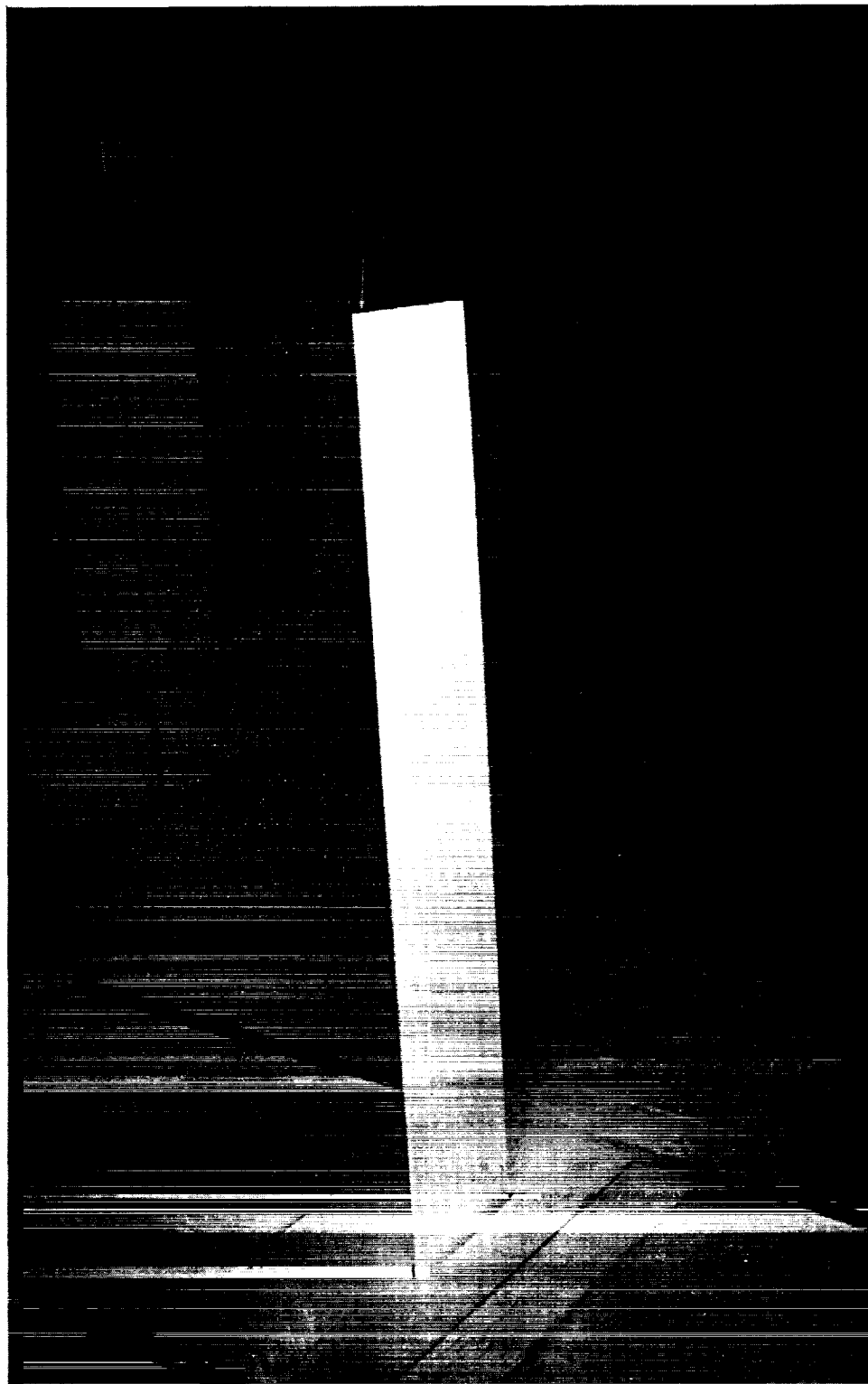
(a) Installation

Figure 3. Semispan wing with deflected tip, in wind tunnel.
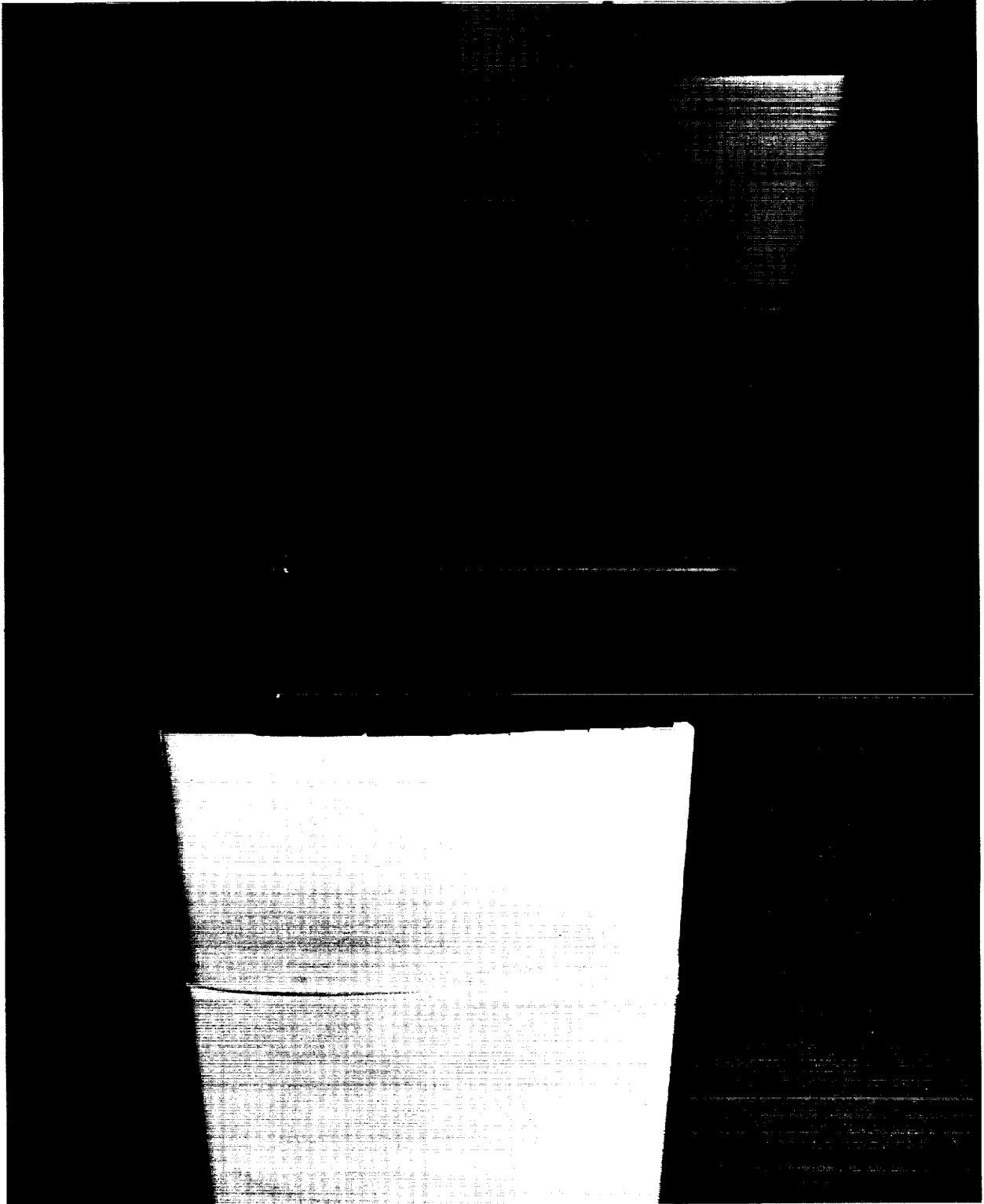
(b) Close-up view

Figure 3. Concluded.
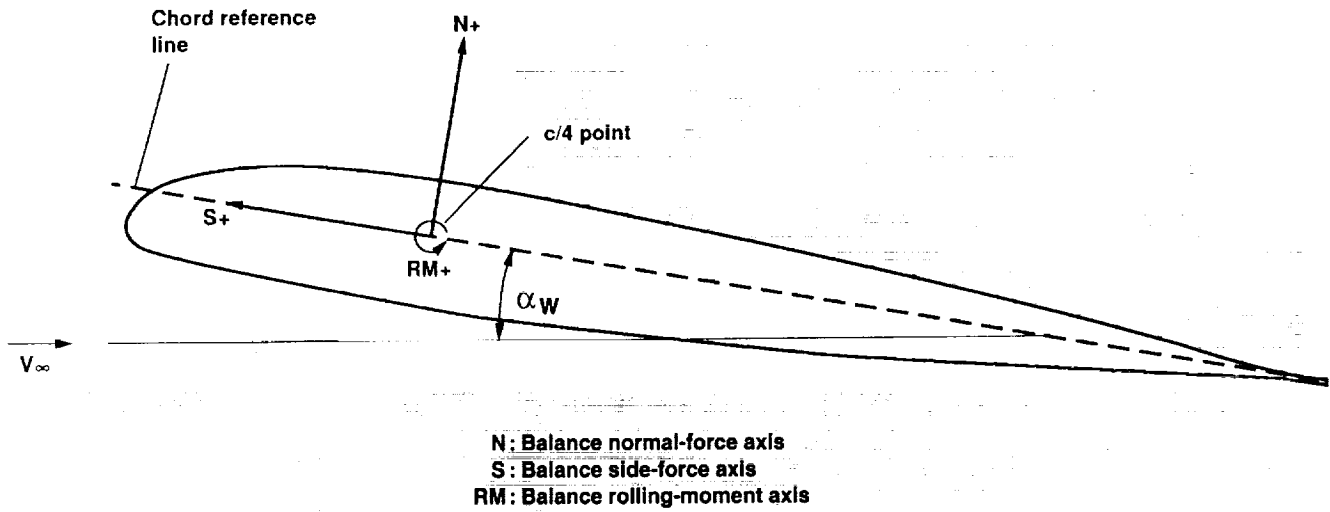
Figure 4. Orientation of internal-balance axis system and V23010 airfoil reference line.

N: Balance normal-force axis
S: Balance side-force axis
RM: Balance rolling-moment axis
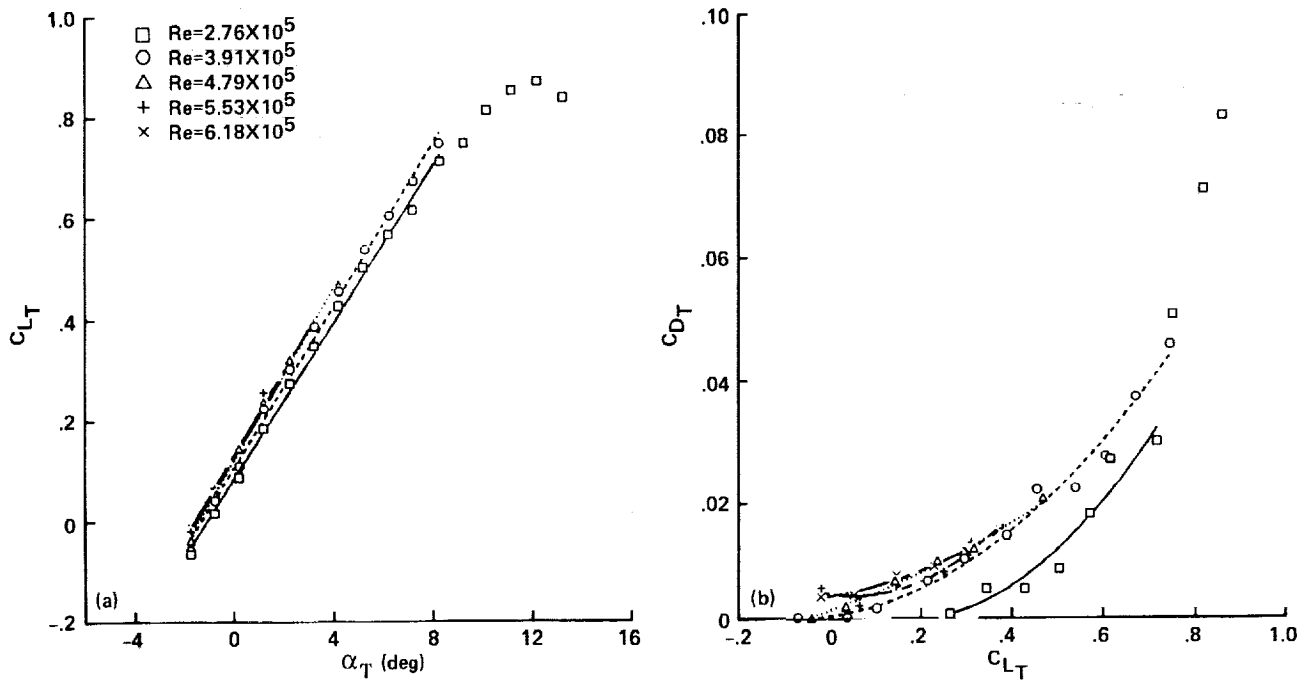
Figure 5. Variation of (a) lift and (b) drag coefficients for the RC10/08 tip, $\Delta\theta = -3.5°$.
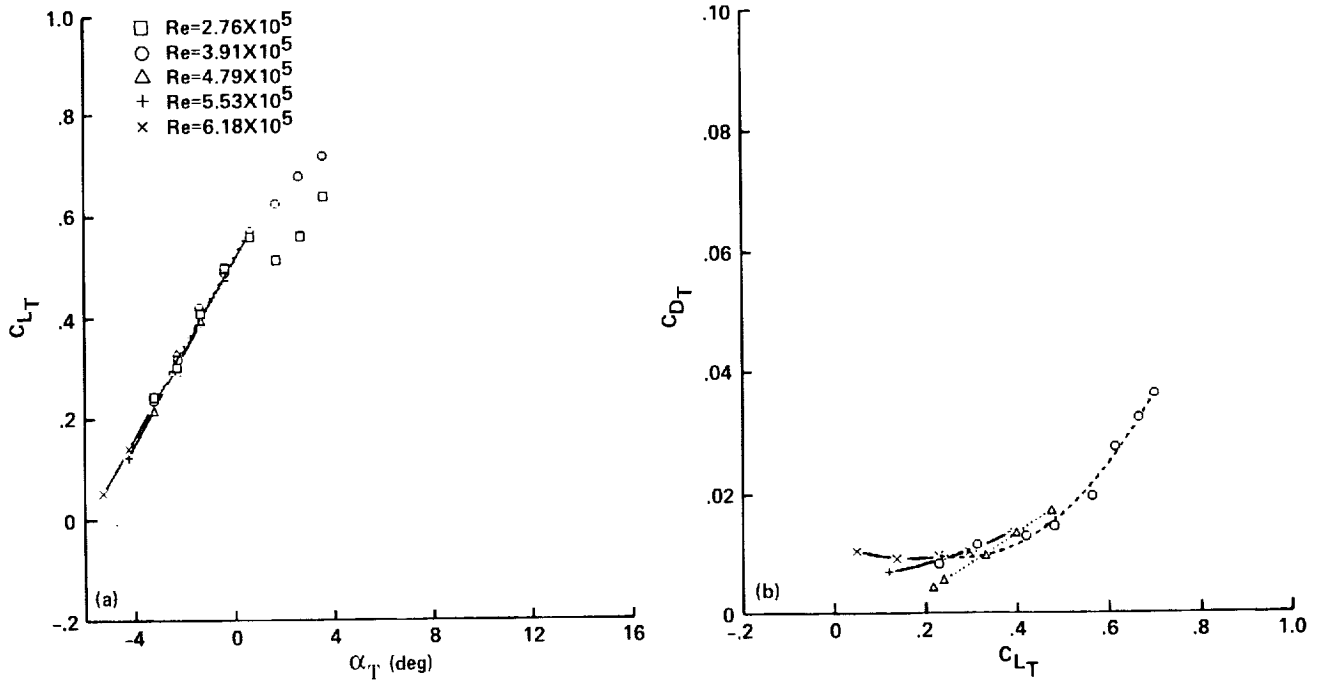
Figure 6. Variation of (a) lift and (b) drag coefficients for the RC10/08 tip, $\Delta\theta = -13.0°$.
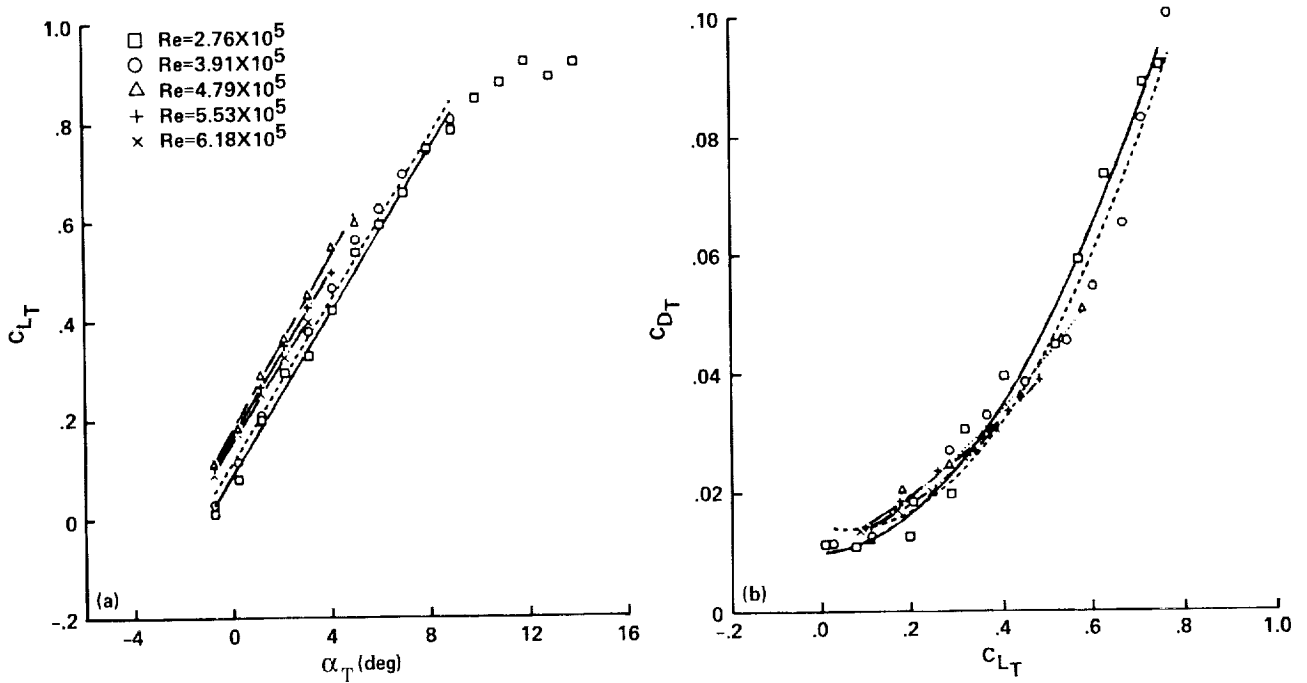
Figure 7. Variation of (a) lift and (b) drag coefficients for the RC10/05 tip, $\Delta\theta = -2.5°$.
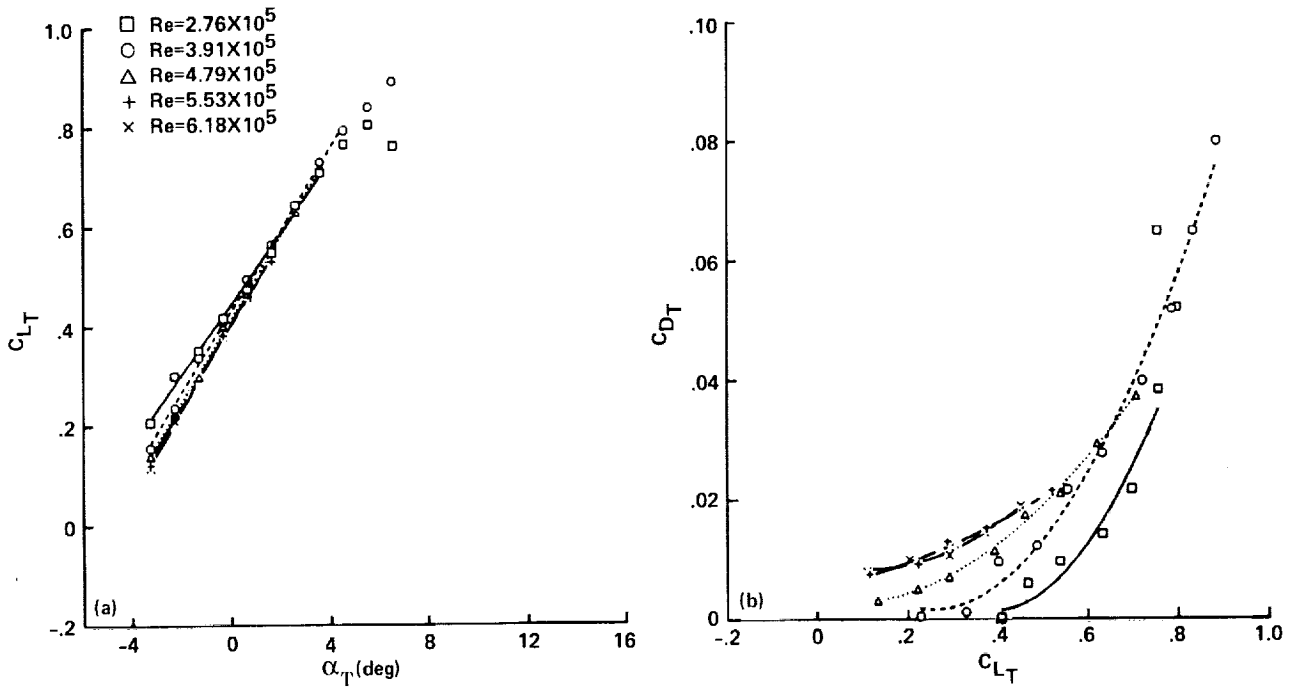
Figure 8. Variation of (a) lift and (b) drag coefficients for the RC10/05 tip, $\Delta\theta = -10.0°$.
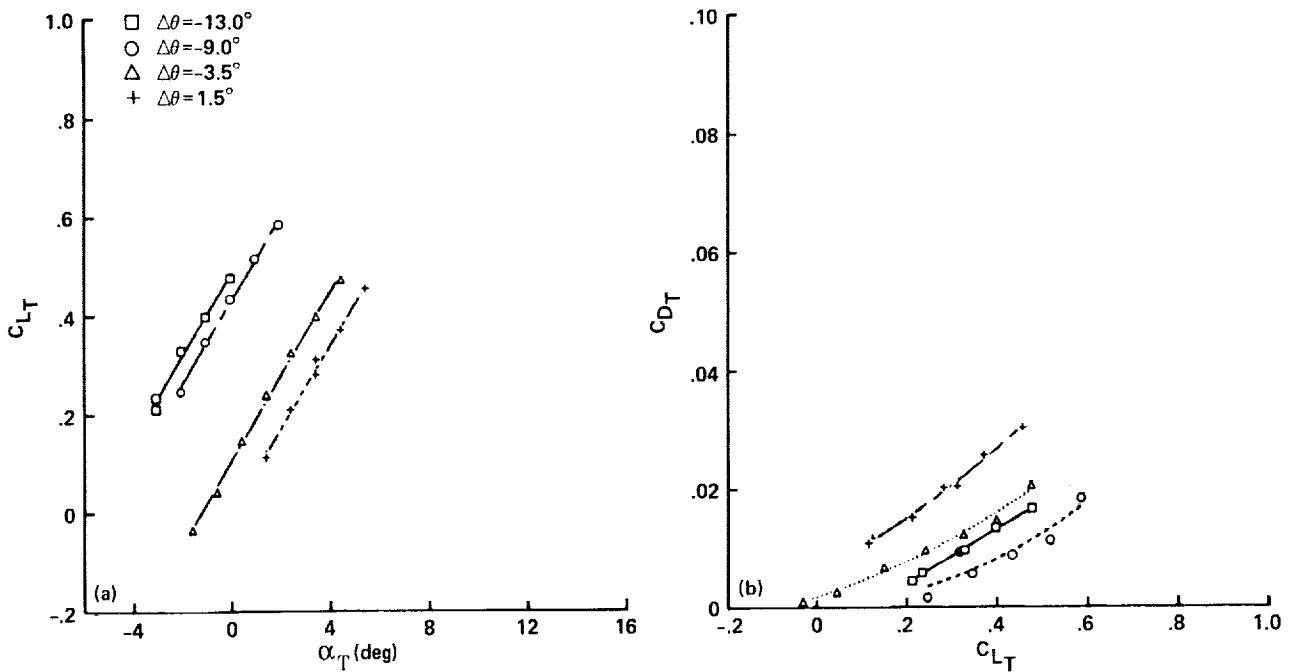
Figure 9. Variation of (a) lift and (b) drag coefficients for the RC10/08 tip, Re = 4.79×10^5.
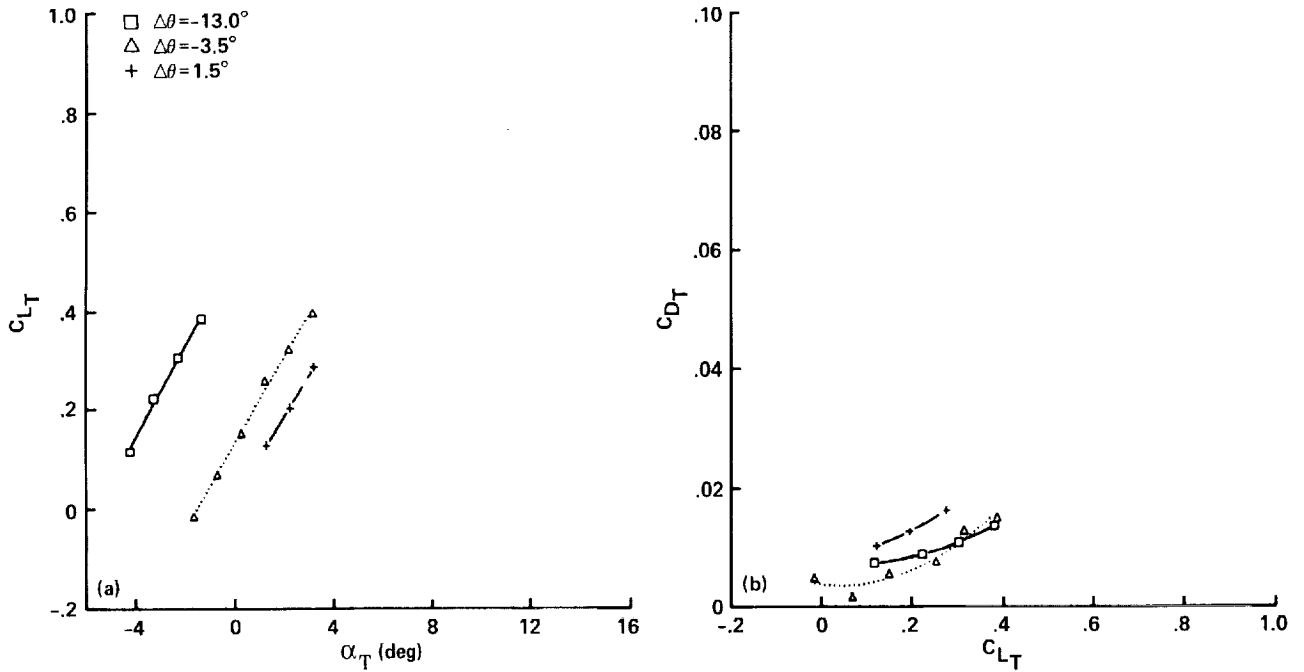
Figure 10. Variation of (a) lift and (b) drag coefficients for the RC10/08 tip, Re = 5.53×10^5.
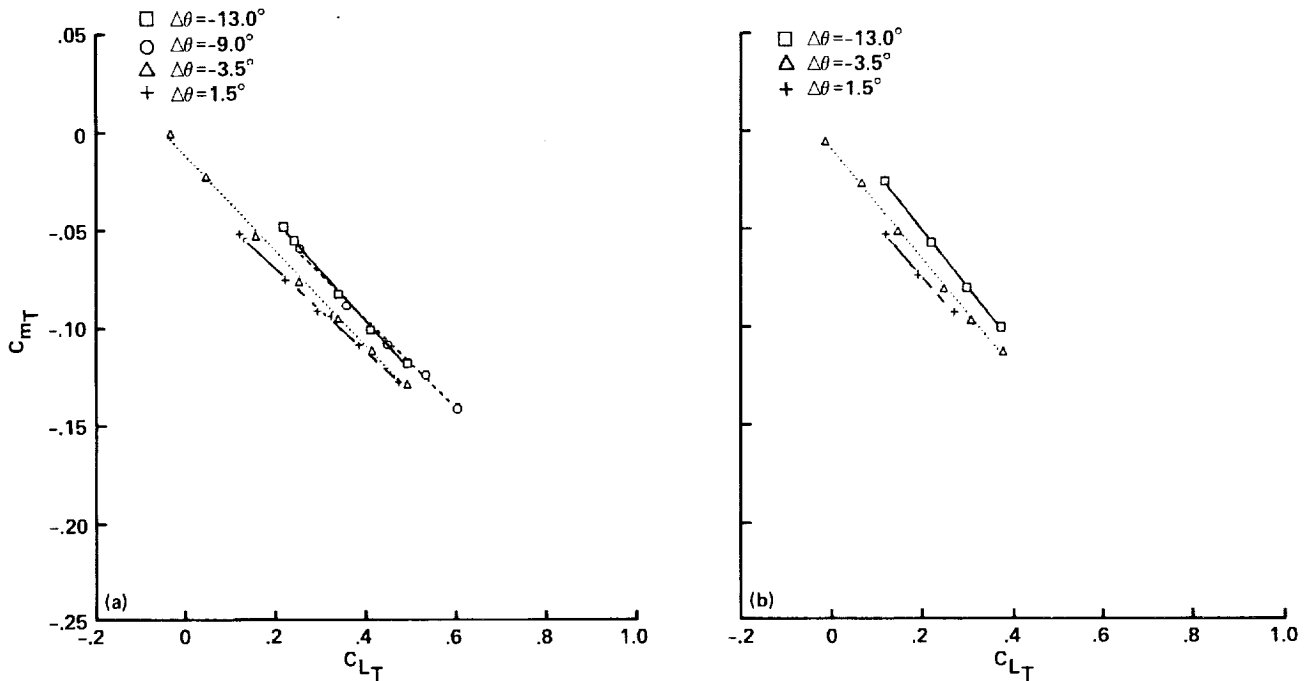
Figure 11. Variation of pitching moment coefficient with lift coefficient for the RC10/08 tip; (a) Re = 4.79×10^5, (b) Re = 5.53×10^5.
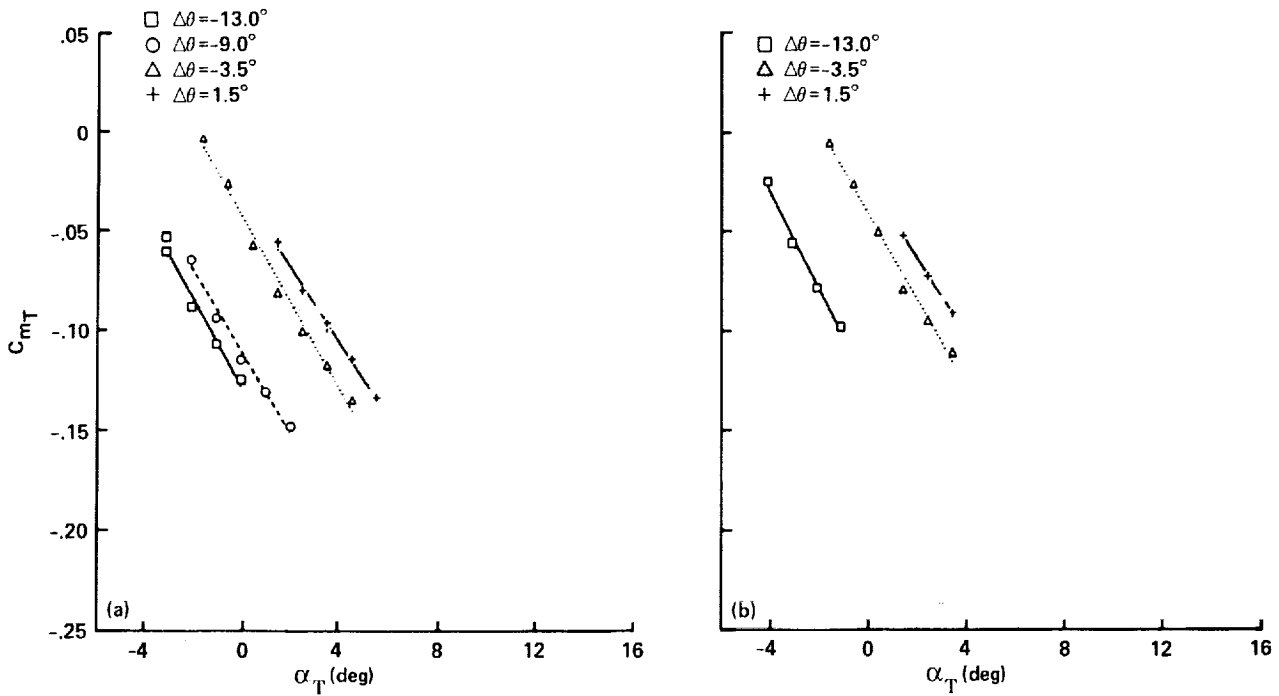
Figure 12. Variation of pitching moment coefficient with angle of attack for the RC10/08 tip; (a) Re = 4.79 × 10⁵, (b) Re = 5.53 × 10⁵.
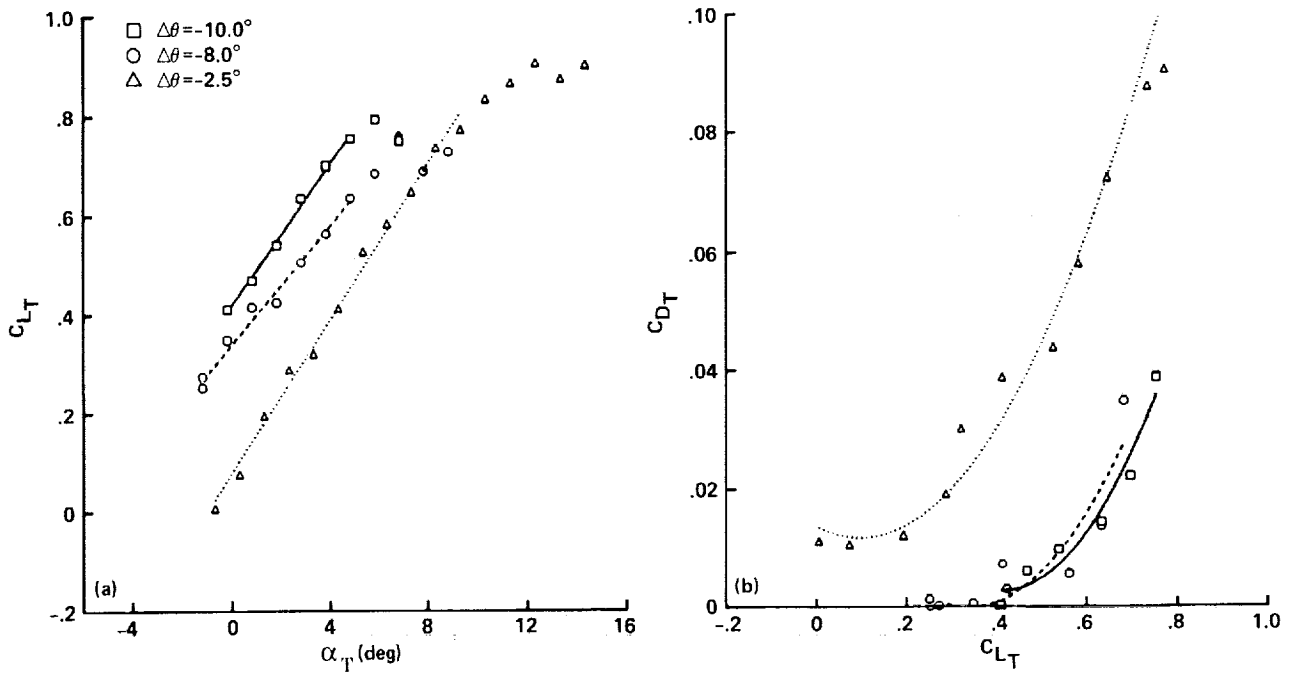
Figure 13. Variation of (a) lift and (b) drag coefficients for the RC10/05 tip, Re = 2.76 × 10⁵.
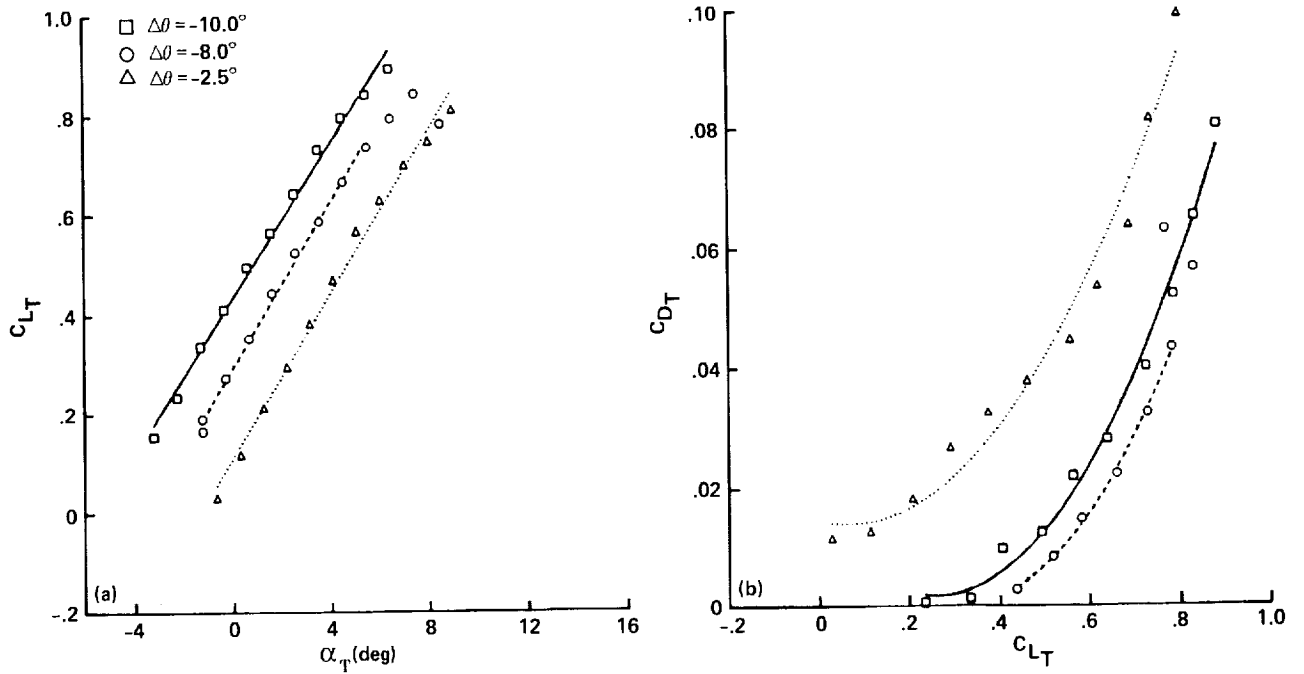
Figure 14. Variation of (a) lift and (b) drag coefficients for the RC10/05 tip, Re = 3.91 × 10⁵.
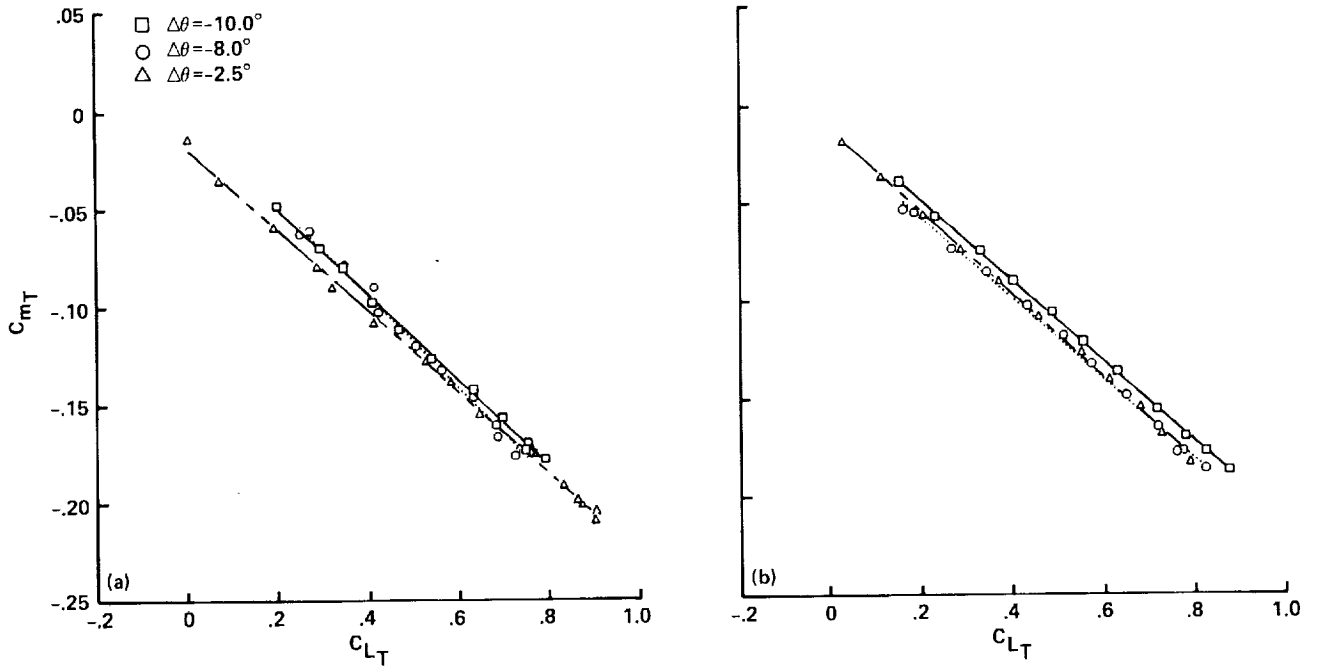
Figure 15. Variation of pitching moment coefficient with lift coefficient for the RC10/05 tip;
(a) Re = 2.76 × 10⁵, (b) Re = 3.91 × 10⁵.
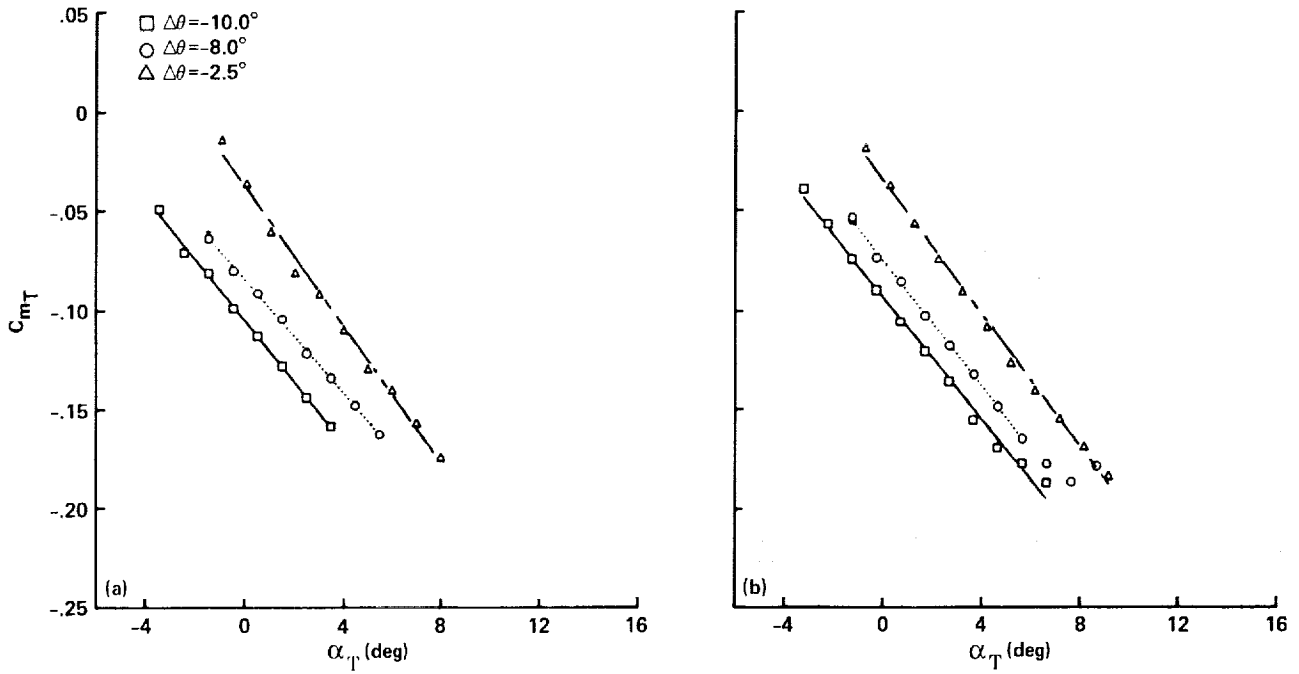
Figure 16. Variation of pitching moment coefficient with angle of attack for the RC10/05 tip; (a) Re = 2.76 × 10⁵, (b) Re = 3.91 × 10⁵.

(a)

(b)

Figure 17. Oil surface flow on the RC10/08 tip; $\alpha_T = -5.0°$, $\Delta\theta = -13.0°$, Re $= 3.91 \times 10^5$; (a) upper surface, (b) lower surface.
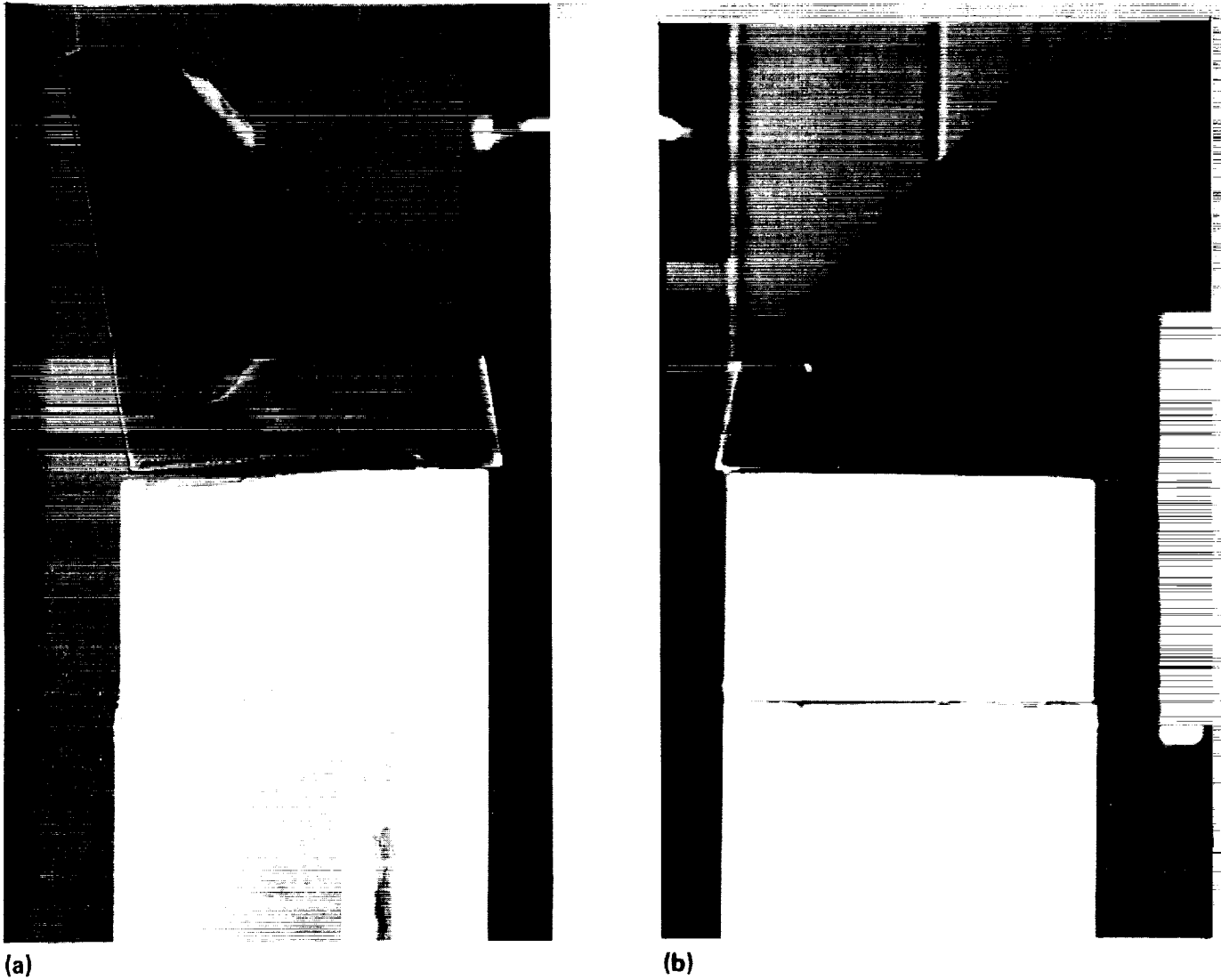
(a)

(b)
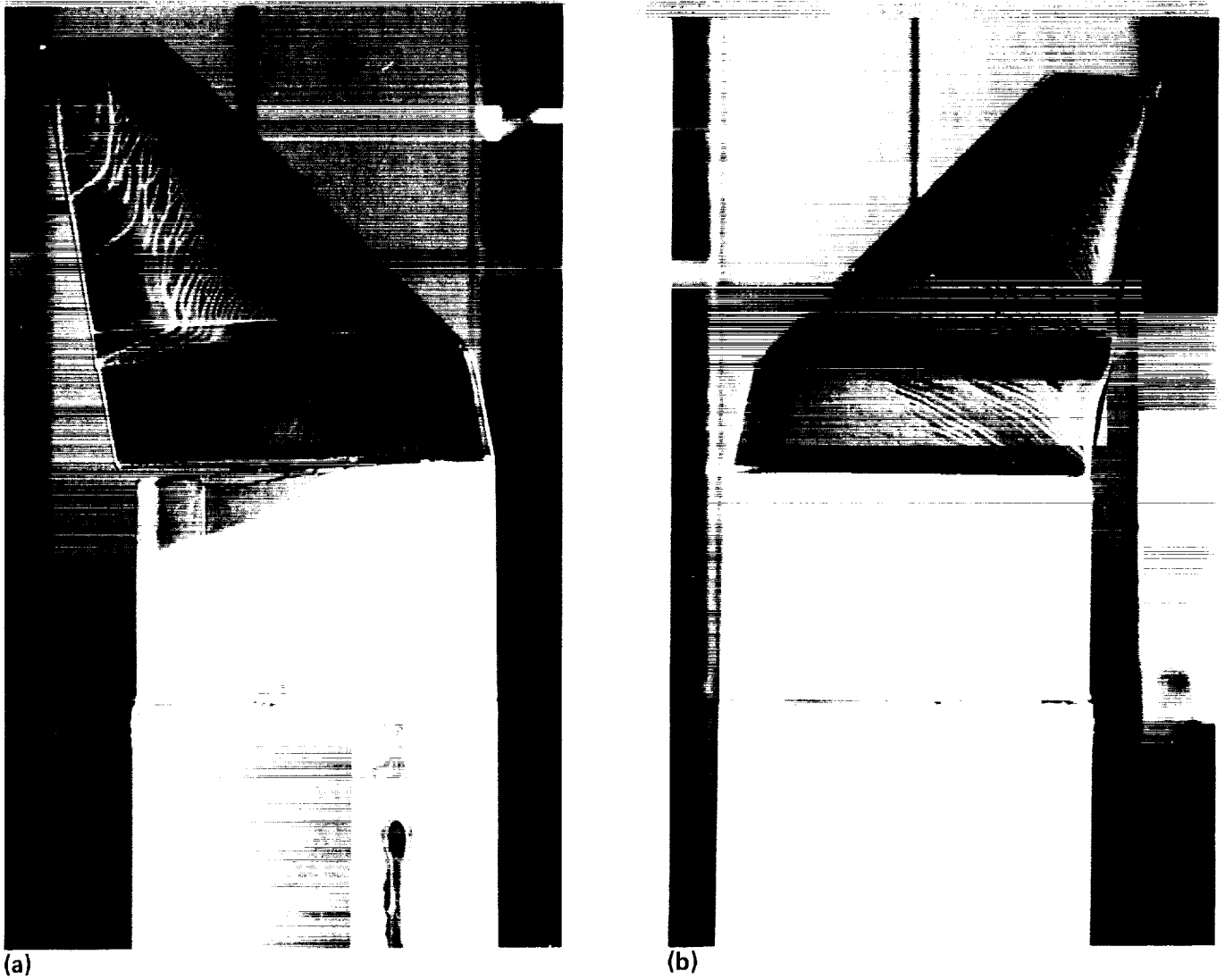
Figure 18. Oil surface flow on the RC10/08 tip; $\alpha_T = -3.0°$, $\Delta\theta = -13.0°$, $Re = 3.91 \times 10^5$; (a) upper surface, (b) lower surface.

46
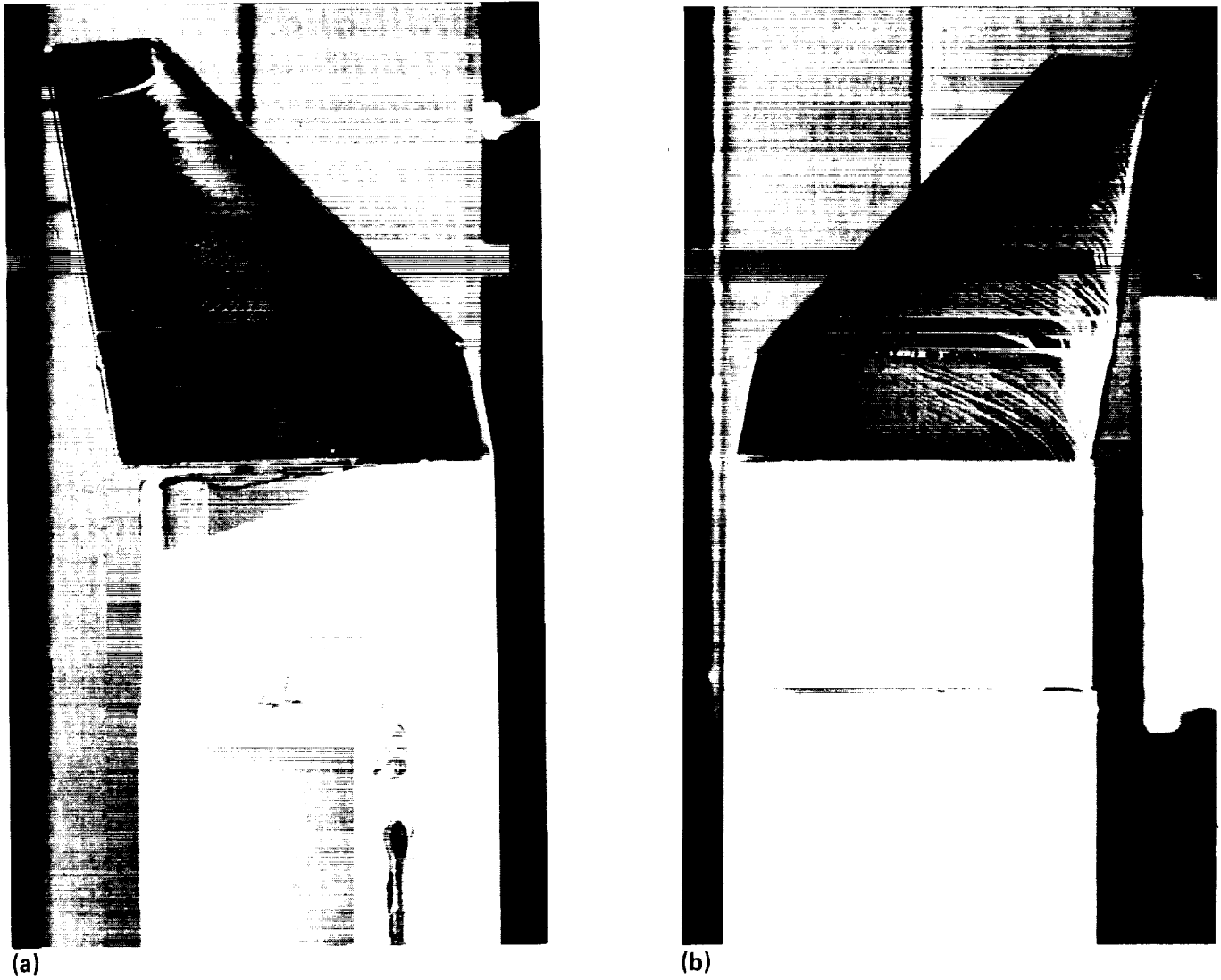
Figure 19. Oil surface flow on the RC10/08 tip; $\alpha_T = -1.0°$, $\Delta\theta = -13.0°$, Re = 3.91×10^5; (a) upper surface, (b) lower surface.

(a)
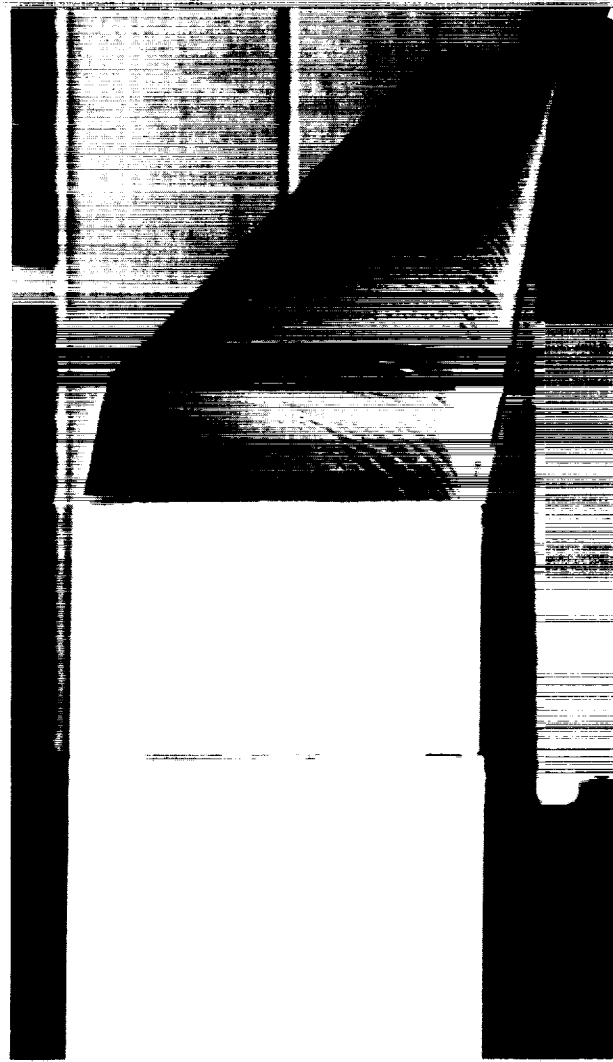
(b)

Figure 20. Oil surface flow on the RC10/08 tip; $\alpha_T = 2.0°$, $\Delta\theta = -13.0°$, Re = 3.91×10^5; (a) upper surface, (b) lower surface.
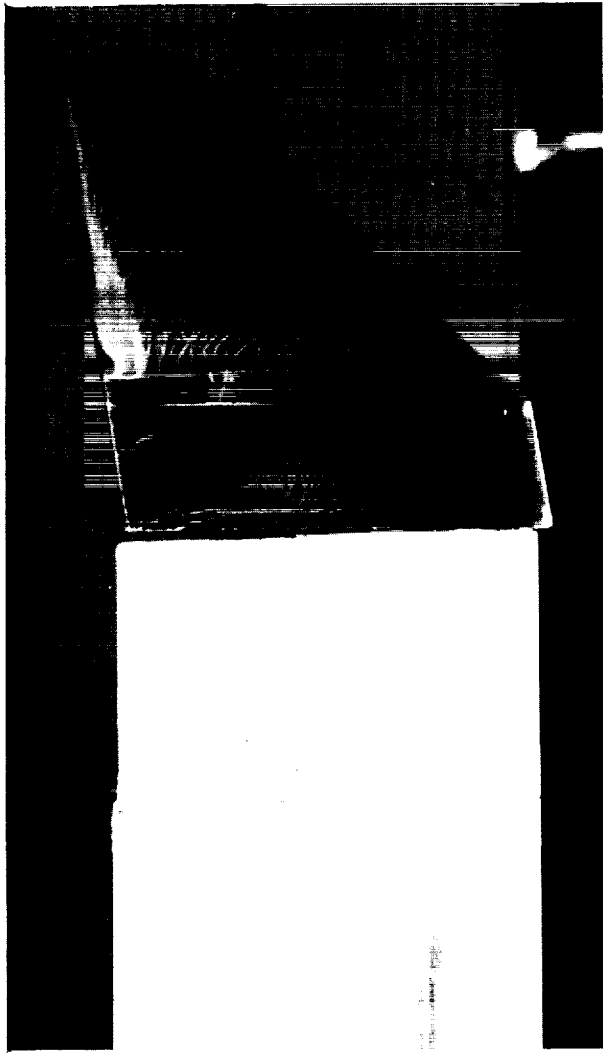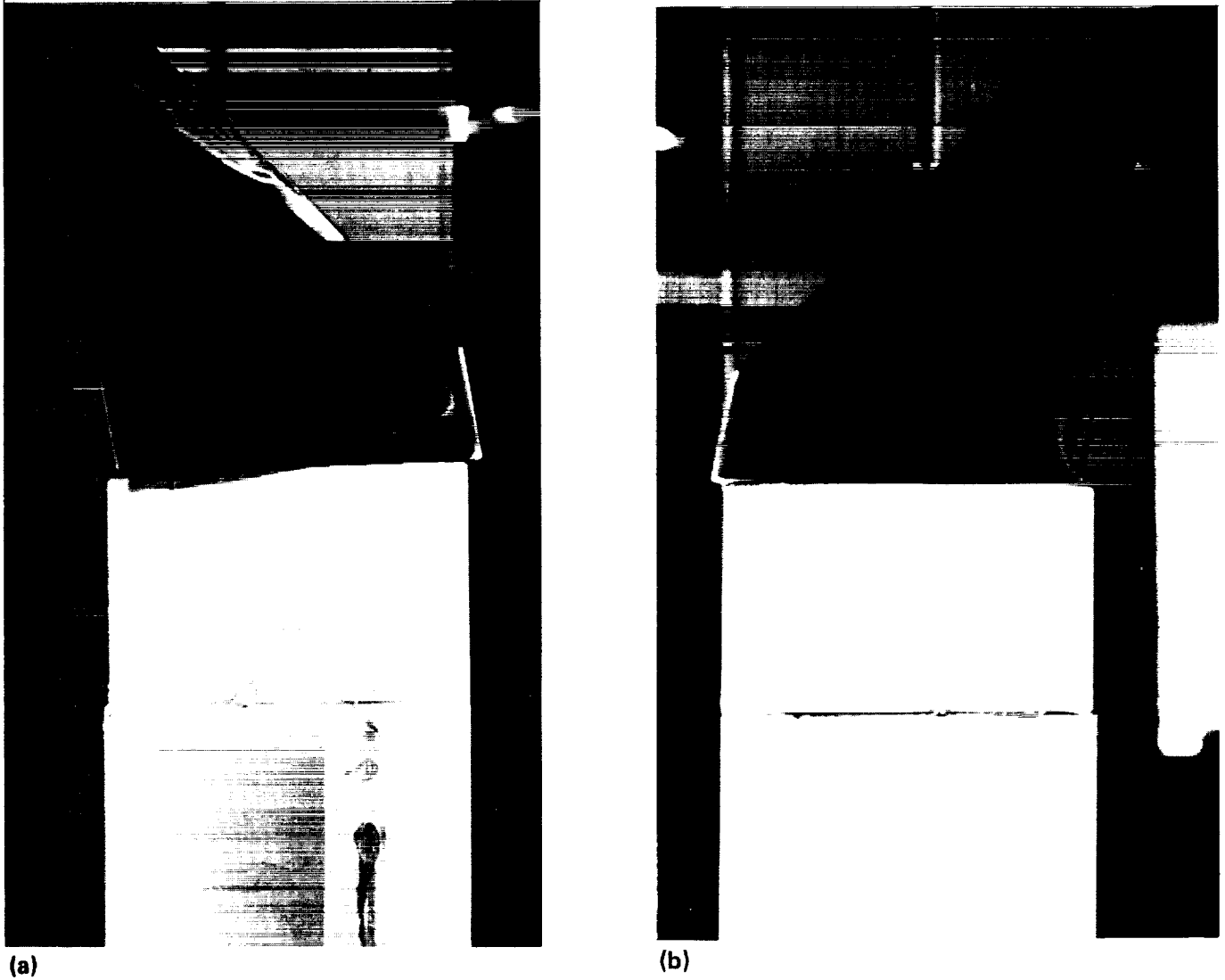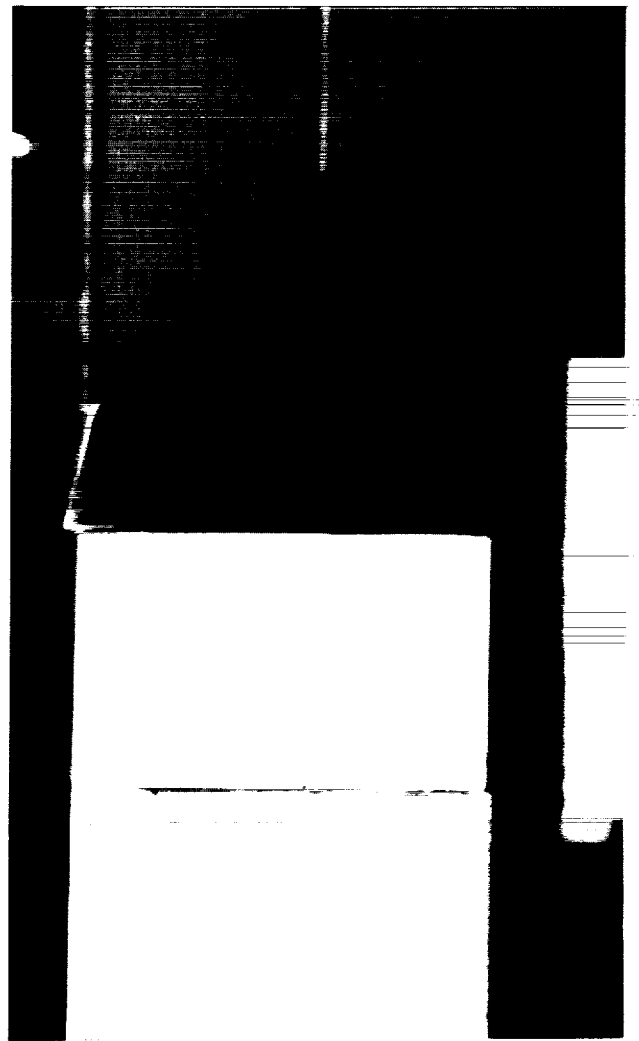
(a)
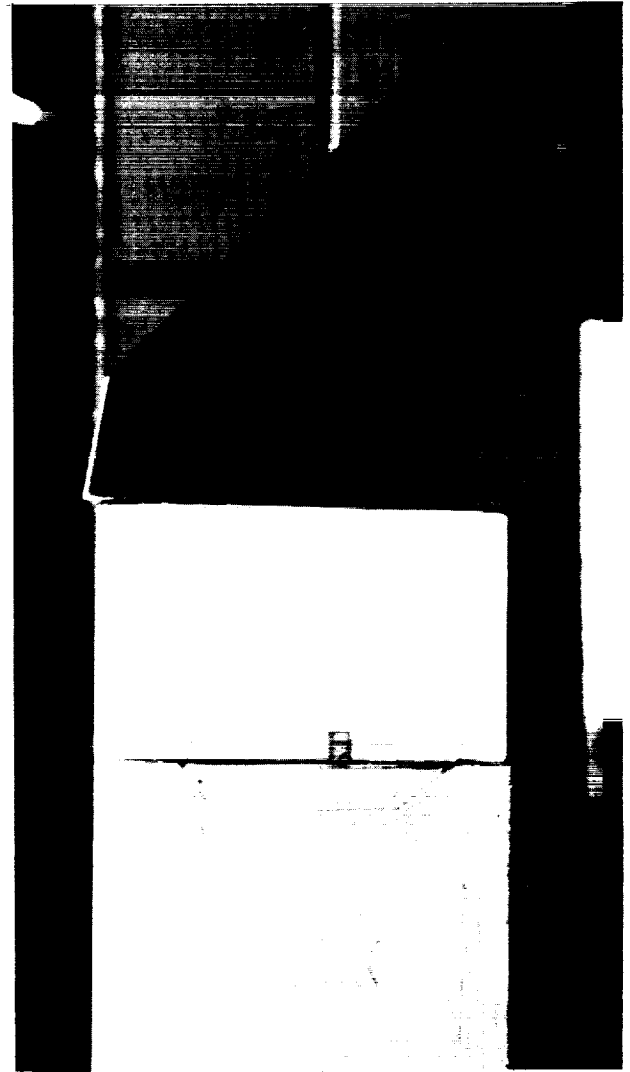
(b)

Figure 21. Oil surface flow on the RC10/05 tip; $\alpha_T = -2.5°$, $\Delta\theta = -2.5°$, Re $= 3.91 \times 10^5$; (a) upper surface, (b) lower surface.

(a)

(b)

Figure 22. Oil surface flow on the RC10/05 tip; $\alpha_T = 2.5°$, $\Delta\theta = -2.5°$, Re = 3.91×10^5; (a) upper surface, (b) lower surface.

(a)

(b)

Figure 23. Oil surface flow on the RC10/05 tip; $\alpha_T = 7.5°$, $\Delta\theta = -2.5°$, $Re = 3.91 \times 10^5$; (a) upper surface, (b) lower surface.

(a)

(b)

Figure 24. Oil surface flow on the RC10/05 tip; $\alpha_T = 12.5°$, $\Delta\theta = -2.5°$, $Re = 3.91 \times 10^5$; (a) upper surface, (b) lower surface.
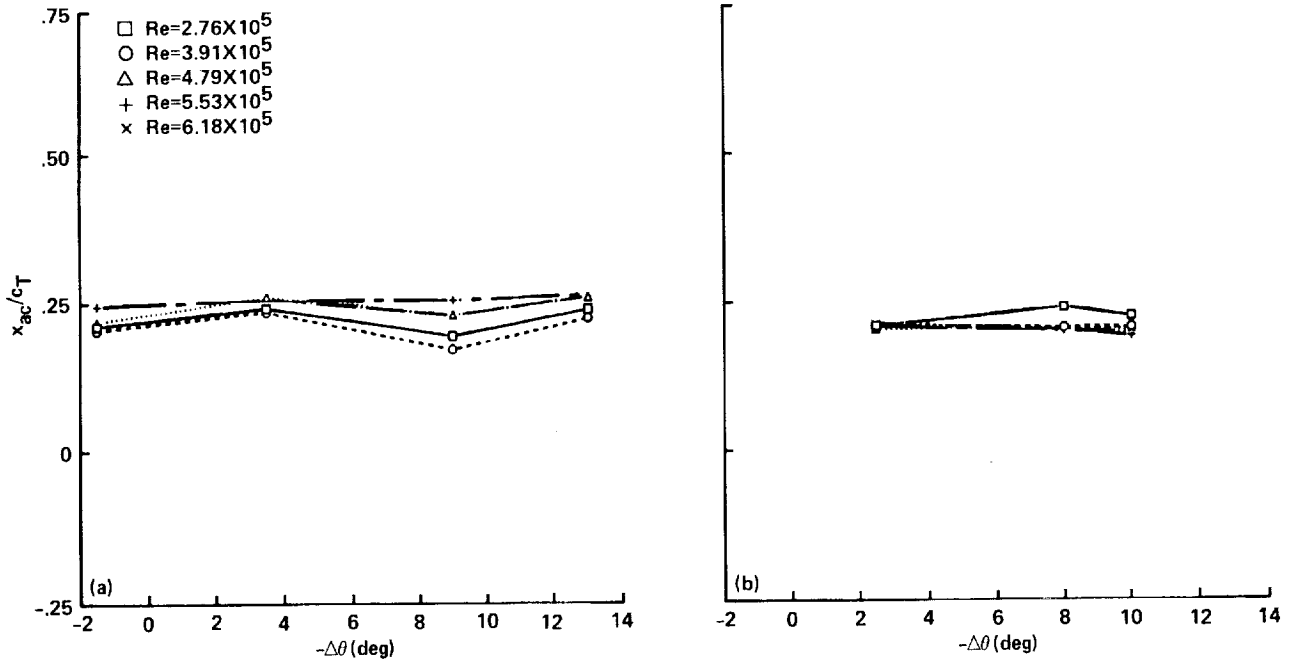
Figure 25. Tip aerodynamic center locations for (a) the RC10/08 tip and (b) the RC10/05 tip in a wing-fixed coordinate system, as a function of $\Delta\theta$.
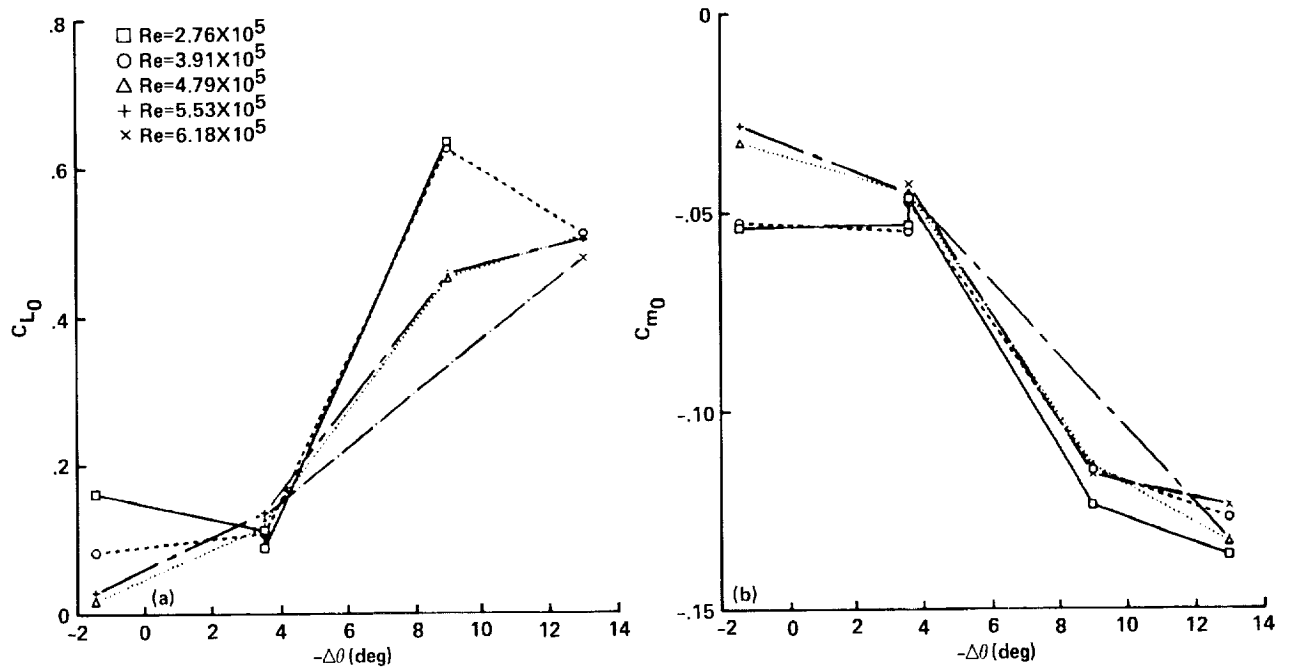

Figure 26. (a) Lift and (b) pitching moment coefficients for the RC10/08 tip as functions of $\Delta\theta$; $\alpha_T = 0°$.
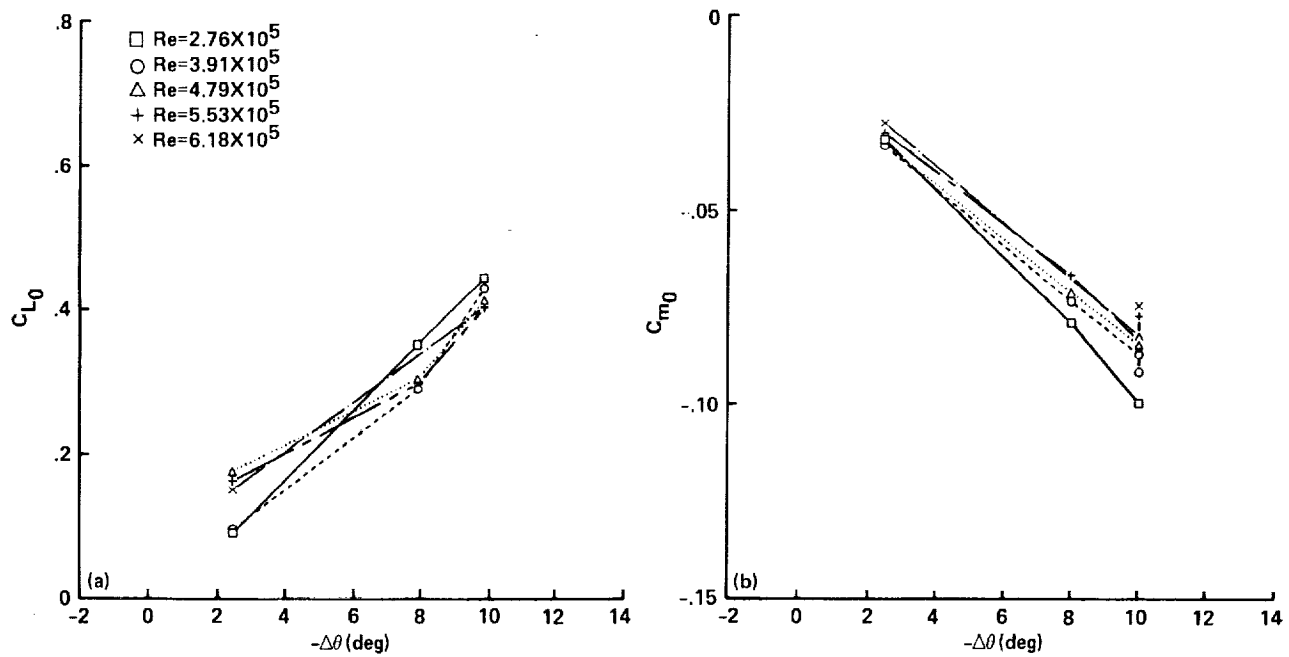
Figure 27. (a) Lift and (b) pitching moment coefficients for the RC10/05 tip as functions of $\Delta\theta$; $\alpha_T = 0°$.

REPORT DOCUMENTATION PAGE

Public reporting burden for this collection of information is estimated to average 1 hour per response, including the time for reviewing instructions, searching existing data sources, gathering and maintaining the data needed, and completing and reviewing the collection of information. Send comments regarding this burden estimate or any other aspect of this collection of information, including suggestions for reducing this burden, to Washington Headquarters Services, Directorate for information Operations and Reports, 1215 Jefferson Davis Highway, Suite 1204, Arlington, VA 22202-4302, and to the Office of Management and Budget, Paperwork Reduction Project (0704-0188), Washington, DC 20503.

1. AGENCY USE ONLY *(Leave blank)*	2. REPORT DATE September 1991	3. REPORT TYPE AND DATES COVERED Technical Memorandum

4. TITLE AND SUBTITLE

Experimental Study of an Independently Deflected Wingtip Mounted on a Semispan Wing

5. FUNDING NUMBERS

RTOP 505-61-51

6. AUTHOR(S)

D. M. Martin (University of Kansas Center for Research, Inc., Lawrence, Kansas) and L. A. Young

7. PERFORMING ORGANIZATION NAME(S) AND ADDRESS(ES)

Ames Research Center
Moffett Field, CA 94035-1000

8. PERFORMING ORGANIZATION REPORT NUMBER

A-90210

9. SPONSORING/MONITORING AGENCY NAME(S) AND ADDRESS(ES)

National Aeronautics and Space Administration
Washington, DC 20546-0001

10. SPONSORING/MONITORING AGENCY REPORT NUMBER

NASA TM-102842

11. SUPPLEMENTARY NOTES

Point of Contact: Daniel M. Martin, Ames Research Center, MS T-042, Moffett Field, CA 94035-1000
(415) 604-4566 or FTS 464-4566

12a. DISTRIBUTION/AVAILABILITY STATEMENT

Unclassified-Unlimited
Subject Category – 02

12b. DISTRIBUTION CODE

13. ABSTRACT *(Maximum 200 words)*

The results of a subsonic wind tunnel test of a semispan wing with an independently deflected tip surface are presented and analyzed. The tip surface was deflected about the quarter-chord of the rectangular wing and accounted for 17% of the wing semispan. The test was conducted to measure the loads on the tip surface and to investigate the nature of aerodynamic interference effects between the wing and the deflected tip. Results are presented for two swept tip surfaces of similar planform but different airfoil distributions. The report contains plots of tip lift, drag, and pitching moment for various Reynolds numbers and tip deflection angles with respect to the inboard wing. Oil flow visualization photographs for a typical Reynolds number are also included. Important aerodynamic parameters such as lift and pitching moment slopes and tip aerodynamic center location are tabulated. A discussion is presented of the relationship between tip experimental data acquired in a steady flow and the prediction of unsteady tip motion at fixed-wing angles of attack.

14. SUBJECT TERMS

Free-tip rotor, Deflected tip, Experimental data

15. NUMBER OF PAGES

64

16. PRICE CODE

A04

17. SECURITY CLASSIFICATION OF REPORT Unclassified	18. SECURITY CLASSIFICATION OF THIS PAGE Unclassified	19. SECURITY CLASSIFICATION OF ABSTRACT	20. LIMITATION OF ABSTRACT

NSN 7540-01-280-5500